A Regional Simulation of Marine Boundary-Layer Clouds

SHOUPING WANG

Universities Space Research Association, NASA/MSFC, Huntsville, Alabama

BRUCE A. ALBRECHT

Department of Meteorology and Earth Science System Center, The Pennsylvania State University, University Park, Pennsylvania

PATRICK MINNIS

Atmospheric Sciences Division, NASA Langley Research Center, Hampton, Virginia

(Manuscript received 15 January 1992, in final form 28 April 1993)

ABSTRACT

A regional version of a two-layer model is used to simulate marine boundary-layer clouds over an area (20°–42°N and 117°–145°W) of the eastern North Pacific. The large-scale conditions required for the model are provided by European Centre for Medium-Range Weather Forecasts analyses and the Comprehensive Ocean–Atmosphere Data Set. The simulated cloud-top height and fractional cloudiness are compared with satellite data. The model predicts a realistic pattern of cloud-top height, although the heights appear to be overestimated in the southwest and underestimated along the eastern border of the domain. The overall simulated cloudiness is qualitatively comparable to the satellite derived, but the model predicts excessive cloudiness over cold ocean surfaces and insufficient cloudiness over an area centered at 30°N, 130°W. The possible causes for these discrepancies are discussed.

Budget studies show that horizontal advection contributes substantially to the cloud-top height and cloud-layer moisture budgets. Thus, one may need to consider the effects of horizontal advection when validating steady-state solutions of a one-dimensional model. The simulated cloudiness is shown to be sensitive to large-scale subsidence, moisture above the clouds, and drizzle. An increase in the large-scale divergence by 2×10^{-6} s^{-1} decreases average cloudiness for the area by 30%. An increase in the moisture at 850 mb by 2 g kg^{-1} increases the cloudiness by 20%. The suppression of drizzle in the model increases the cloudiness by 34% and significantly changes its pattern.

1. Introduction

A one-dimensional two-layer model of marine boundary-layer (MBL) clouds is described in Wang (1993). This model not only predicts the boundary-layer thermodynamic structure but also provides fractional cloudiness for marine stratocumulus and trade-wind cumulus clouds, a generality that is not available from classic mixed-layer models (Lilly 1968). In this study, we extend this one-dimensional model to a regional version and use this regional model to simulate marine boundary-layer clouds over the eastern North Pacific.

A successful development of a boundary-layer parameterization depends not only on the development of a coherent formulation of convective and radiative processes, but also on the validation and evaluation of results against observations. It is difficult, however, to verify and evaluate a one-dimensional model, since it neither includes horizontal advection nor provides a horizontal distribution of cloud characteristics.

Usually, the validation and evaluation of a boundary-layer model are based on the comparison between simulated and observed structures. Over oceans, however, no routine observations are available. Only a few field experiments offer limited observational data. Satellite images, however, provide large-scale features of boundary-layer clouds such as horizontal distribution of fractional cloudiness and cloud-top heights (Heck et al. 1990) that can be used for the verification of boundary-layer models. In addition, a boundary-layer model is essentially driven by large-scale conditions such as sea surface temperature, large-scale subsidence, and thermodynamic structure above the boundary layer; thus, it is critical to know how sensitive the simulated clouds in the boundary-layer model are to these large-scale parameters. Furthermore, it is our hope that the boundary-layer model described by Wang (1993) could be eventually implemented into a general circulation model. Thus, the formulations of the cloud

Corresponding author address: Dr. Shouping Wang, Universities Space Research Association, NASA/MSFC, ES-42, Huntsville, AL 35812.

variables that are crucial for climate studies, such as fractional cloudiness, should be verified against data. Therefore, it is important to compare results from the regional model with satellite-derived cloud fields.

In addition, the regional simulation approach provides a framework for defining detailed boundary-layer structure from coarse-resolution global analyses and satellite data. Betts et al. (1992) demonstrated how boundary-layer structure could be defined along a trajectory, where cloud-top temperature and cloud cover were constrained by satellite observations. We could also use satellite data to constrain the regional model variables, such as cloud-top heights and precipitable water content, to diagnose and define marine boundary-layer structures and surface fluxes that are not directly available from satellite observations. For example, Robertson and Cohen (1990) combined data from Special Sensor Microwave Imager (SSM/I) and a simple cloud microphysical model to diagnose global vertical moisture structure. This method has direct implications for application of future satellite data.

Wakefield and Schubert (1981), using a trajectory approach, simulated a stratocumulus boundary layer over the eastern North Pacific. They showed that satellite data is very useful for verification of an MBL model. In this paper, we use a regional version of the two-layer model described in Wang (1993) with the large-scale conditions provided by the ECMWF analyses to simulate the boundary-layer clouds in the eastern North Pacific observed during the First International Satellite Cloud Climatology Project Regional Experiment (FIRE) period (Albrecht et al. 1988). The model results are compared with those derived from satellite data from the Geostationary Operational Environmental Satellite (GOES). Budget studies are conducted to define the relative importance of different processes that maintain the cloud and boundary-layer structure. The sensitivity of the simulated cloudiness to the specification of some large-scale conditions and drizzle is also evaluated.

2. The regional model

The one-dimensional model described by Wang (1993) is extended to a regional version. The vertical structure and the formulation of convective fluxes of the regional model are identical to those in Wang (1993). The model vertical structure, as shown in Fig. 1, consists of a subcloud and a cloud layer. The cloud layer is capped by an inversion with an infinitesimally thin thickness. The simulated clouds may have a partial or full fractional coverage depending on the thermodynamic structure of the cloud layer. When the mean condition in the cloud layer becomes saturated, solid stratiform clouds can top scattered cumulus clouds and thus have bases that are higher than cumulus cloud bases. The term *cloud-base level* (z_c) used in this paper refers to the scattered cumulus cloud base. The cloud and subcloud layers are separated by a stable layer that is infinitesimally thin. This cloud-base stable layer regulates the coupling between the cloud and subcloud layer in the model. It should be stressed that this infinitesimally thin stable layer exists at the same level as z_c; thus, decoupling always occurs below the base level of solid clouds as shown in Fig. 1. The subcloud layer is assumed to be well mixed in the sense that all conserved thermodynamic variables such as total water (q), moist static energy (h), liquid water dry static energy ($s_L = h - Lq$), and liquid water potential temperature ($\theta_L = s_L/c_p$) do not vary with height. In the cloud layer, h and q are assumed to be a linear function of height. Therefore, the mean boundary-layer structure is fully defined by the eight variables: q_M, h_M, q_B, h_B, q_i, h_i, z_c, and z_i, where subscripts M, B, and i denote the values in the subcloud layer, at cloud-base level, and cloud-top level, respectively, and z_i and z_c are cloud-top and cloud-base level, respectively.

a. The predictive equations

For a regional simulation of MBL, the predictive equations may be written as follows:

$$\frac{\partial \overline{q_M}}{\partial t} = -\nu_0 \cdot \nabla \overline{q_M} - \frac{\overline{w'q'_B} - \overline{w'q'_0}}{z_c} - \text{Eva} - K\nabla^2 \overline{q_M} \tag{1}$$

$$\frac{\partial \overline{h_M}}{\partial t} = -\nu_0 \cdot \nabla \overline{h_M} - \frac{\overline{w'h'_B} - \overline{w'h'_0}}{z_c} - \left(\frac{\partial F_R}{\partial z}\right)_M - K\nabla^2 \overline{h_M} \tag{2}$$

$$\frac{\partial \overline{q_B}}{\partial t} = -\nu_0 \cdot \nabla \overline{q_B} + \gamma_q \left(\frac{dz_c}{dt} - w_D\right) - \left(\frac{\partial \overline{w'q'}}{\partial z}\right)_B + K\nabla^2 \overline{q_B} \tag{3}$$

$$\frac{\partial \overline{h_B}}{\partial t} = -\nu_0 \cdot \nabla \overline{h_B} + \gamma_h \left(\frac{dz_c}{dt} - w_D\right) - \left(\frac{\partial \overline{w'h'}}{\partial z}\right)_B - \left(\frac{\partial F_R}{\partial z}\right)_B + K\nabla^2 \overline{h_B} \tag{4}$$

$$\frac{\partial \overline{q_i}}{\partial t} = -\nu_0 \cdot \nabla \overline{q_i} + \gamma_q \left(\frac{dz_i}{dt} - w_D\right) - \left(\frac{\partial \overline{w'q'}}{\partial z}\right)_i - \text{Pre} + K\nabla^2 \overline{q_i} \tag{5}$$

$$\frac{\partial \overline{h_i}}{\partial t} = -\nu_0 \cdot \Delta \overline{h_i} + \gamma_h \left(\frac{dz_i}{dt} - w_D\right) - \left(\frac{\partial \overline{w'h'}}{\partial z}\right)_i + \left(\frac{\partial F_R}{\partial z}\right)_i + K\nabla^2 \overline{h_i} \tag{6}$$

$$\frac{\partial z_i}{\partial t} = \nu_0 \cdot \nabla z_i + w_{ei} + w_D + K\nabla^2 z_i. \tag{7}$$

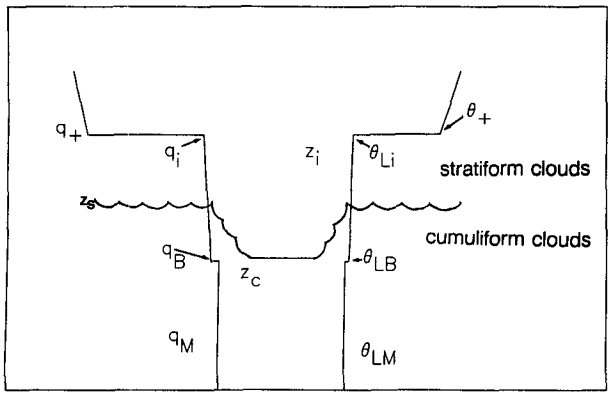

FIG. 1. The vertical structure of the two-layer boundary-layer model.

In the above equations, subscript 0 denotes the quantity at the sea surface. The symbol F_R denotes radiative fluxes, Eva the evaporation rate in the subcloud layer, Pre the precipitation in the cloud layer, γ_q and γ_h are the gradients of q and h in the cloud layer, w_{ei} is the entrainment velocity at the top of the boundary layer, and w_D is large-scale subsidence assumed to be linear with height. The gradients in the cloud layer are calculated from $\gamma_\varphi = (\overline{\varphi_i} - \overline{\varphi_B})/(z_i - z_c)$, where φ represents either q or h. A horizontal diffusion term with coefficient K is added in every equation to represent horizontal small-scale mixing and to improve numerical stability. The cloud base is assumed to be at the same level as the lifting condensation level (LCL) of a surface air parcel.

b. *The convective fluxes*

The surface fluxes are calculated using the common bulk method with a transfer coefficient $C = (1 + 0.07v_0) \times 10^{-3}$ (Wakefield and Schubert 1981). The fluxes at the top of the mixed layer are defined as

$$\overline{w'\varphi'_1} = \frac{\Delta_B\bar{\varphi}}{\Delta_B\bar{s}_v}\overline{w's'_{v_1}}, \tag{8}$$

where Δ_B denotes the jump across the cloud-base stable layer and s_v is virtual dry static energy. The buoyancy flux at the top of the mixed layer $\overline{w's'_{v_1}}$ is taken to be -0.2 of the surface buoyancy flux.

The convective fluxes in the cloud layer are parameterized with the mass flux representation,

$$\overline{w'\varphi'} = \frac{\omega^*}{1 - \sigma_u}(\varphi_u - \bar{\varphi}), \tag{9}$$

where ω^* is the convective mass flux and σ_u the updraft fractional area. In this formulation ω^* and $(\varphi_u - \bar{\varphi})$ are expressed as linear functions of height, that is,

$$\omega^* = \omega^*_B[1 + \mu(z - z_c)] \tag{10}$$

and

$$(\varphi_u - \bar{\varphi}) = (\overline{\varphi_M} - \overline{\varphi_B})[1 + \lambda_\varphi(z - z_c)], \tag{11}$$

where ω^*_B is the mass flux at the cloud base, λ_φ is defined by a bulk model for updrafts, μ is determined by considering a life cycle of a cloudy updraft (Albrecht et al. 1979):

$$\mu = \frac{E}{z_i - z_c} - \frac{1 + 0.67E}{2\omega^*_B\tau_{\text{adj}}}, \tag{12}$$

where E is a lateral entrainment factor determined using the method of Wang (1992), and $\tau_{\text{adj}} = \frac{1}{3}$ day as used in Albrecht et al. (1979). The updraft fraction, σ_u, is assumed constant with height and determined by $\sigma_u = 0.5e^{-\text{Ri}^{1/2}}$ as in Wang (1993), where Ri is the Richardson number calculated across the cloud-base stable layer. The mass flux at the cloud base, ω^*_B, is obtained by assuming that the mixed-layer height is the same as the cloud-base height, which is the lifting condensation level of a mixed-layer parcel.

The entrainment velocity at the cloud-top inversion is determined by

$$w_{ei} = \frac{-(\overline{w's'_L})_i + \Delta(F_R)_i}{\Delta(s_L)_i}, \tag{13}$$

where $\Delta(\phi)_i$ is the jump across the inversion in variable ϕ.

The drizzle parameterization follows that of Arakawa and Schubert (1974) and Albrecht (1993). The drizzle flux divergence is $\text{Pre} = -c_0\omega^*q_{L_c}$, where q_{L_c} is the liquid water content in the parameterized clouds and c_0 is a efficiency constant for drizzle production. For the evaporation term in Eq. (1), the following formula is used (Sundqvist 1978):

$$\text{Eva} = -(1 - \text{RH}_M)\frac{\int_{z_c}^{z_i} c_0\omega^*q_{L_c}dz}{z_c}, \tag{14}$$

where RH_M is the mean relative humidity of the subcloud layer. Therefore, the drizzle rate at the surface is determined from $\text{RH}_M\int_{z_c}^{z_i} c_0\omega^*q_{L_c}dz$.

c. *Cloud fraction*

The cloud fraction, or cloud cover, is calculated as in Albrecht (1983) and Wang (1993):

$$\sigma_t = \sigma_u + (1 - \sigma_u)\frac{\text{RC} - 1}{\text{RC} - \text{RH}}, \tag{15}$$

where $\text{RC} = q_u/\overline{q_s}$ and $\text{RH} = \bar{q}/\overline{q_s}$. It is clear that in this formulation, cloud cover strongly depends on the mean relative humidity of environment in the cloud layer. If the mean condition of the cloud layer becomes saturated (i.e., $\bar{q} = \overline{q_s}$), the cloud cover is 100%, indicating that stratiform clouds have formed.

d. Radiation calculation

The radiation calculation for the regional model is the same as that of the one-dimensional version in Wang (1993) except that the empirical formula of downward longwave radiative flux of Wakefield and Schubert (1981) is used to give the downward flux at a level of 3 km. The longwave radiative cooling rate of clear air and the downward longwave radiative flux at the cloud top are calculated using the emissivity method (Rogers 1967) with 100-m sublayers from the surface to 3 km. The analytic formulation for longwave and shortwave radiative fluxes of Hanson and Derr (1987) is used to calculate radiative heating rate inside clouds and the total divergence in the cloud-top inversion. An excursion layer with 50-m thickness is assumed at the top of the boundary layer. The bulk cloud optical properties for shortwave radiation calculation are computed using the parameterization of Stephens et al. (1984). The clear air longwave radiation is calculated every 5 hours to avoid a considerable increase in computation time. In the radiation calculation here, no attempt is made to include the direct influence of radiation on the stability of the cloud layer (i.e., $\partial^2 F_R/\partial z^2 = 0$), although radiation may significantly vary the stability of the boundary layer by inhomogeneous heating between the cloud and subcloud layer. Therefore, the uniform longwave and shortwave heating rate in the cloud layer can be written as follows:

$$\frac{\partial F_R}{\partial z} = \frac{1}{z_i - z_c}\int_{z_c}^{z_i}\left[\left(\frac{\partial F_R}{\partial z}\right)_{\text{cloud}}\sigma_t + \left(\frac{\partial F_R}{\partial z}\right)_{\text{clear}}(1-\sigma_t)\right]dz. \quad (16)$$

3. Large-scale conditions for the simulations

The boundary-layer model is applied to the region of 20°–42°N, 117°–145°W for 29 June–19 July 1987, the period of FIRE marine stratocumulus intensive field observations (IFO) (Albrecht et al. 1988). In this study, the land area is neglected for simplicity. Averaged large-scale fields over this period from the ECMWF analyses are used to provide upper and lower boundary conditions for the model. The wind at 1000 mb and the simulated domain are shown in Fig. 2. Close to the coast of the United States the wind direction is either approximately along the coastline or directed out of the domain. Thus, the mean marine boundary-layer structure should not be strongly affected by the conditions over land for this case and the neglect of land area is justified. For simplicity, the wind field at 1000 mb is used for calculations of the horizontal advection for both the cloud and subcloud layers, although it is possible that wind varies with height in the MBL. The pressure field presented in Fig. 3a shows a subtropical high centered over the northwest

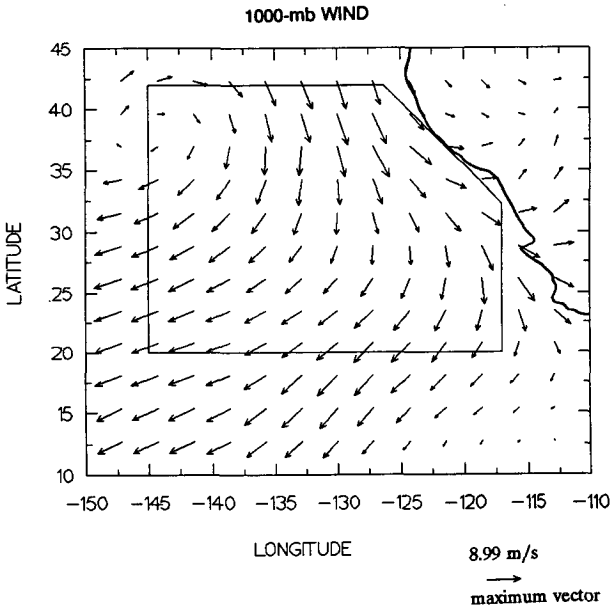

FIG. 2. Mean wind at 1000 mb over 29 June–20 July 1987 (the FIRE period) defined from the ECMWF analyses. The inner area is the area simulated with the model.

corner of the domain. The 700-mb water vapor mixing ratio from the ECMWF analyses is shown in Fig. 3b. The 850-mb water vapor mixing ratio from the ECMWF analyses is found to be considerably higher than that observed from aircraft during FIRE. For example, the ECMWF analyses give 8–10 g kg^{-1} at 850 mb for the entire simulated domain, compared with only 3 g kg^{-1} at the same level from the averaged sounding of FIRE. It is seen that the 700-mb moisture from the ECMWF analyses is more consistent with that observed at 850 mb. Since no other observations are available, it is assumed that the moisture at 850 mb is the same as that at 700 mb. In general, however, the moisture field at this level must be viewed as uncertain. The moist static energy at 850 mb and 700 mb used in the model is shown in Fig. 4. The conditions just above the boundary-layer top are derived by interpolation or extrapolation of input at the layers of 700 mb and 850 mb, that is,

$$h_+ = h_{850} + \frac{h_{700} - h_{850}}{z_{700} - z_{850}}(z_i - z_{850}), \quad (17)$$

where the numbers in the subscripts denote the pressure level and "+" indicates the level just above the inversion.

The July mean sea surface temperature (SST) used in this study is obtained from COADS (Hanson 1990, personal communication) and is shown in Fig. 5a. The minima in the SST field (14°C) are located near the coast and the northwest corner of the domain. Another local minimum is at 27°N, 135°W. The mean large-

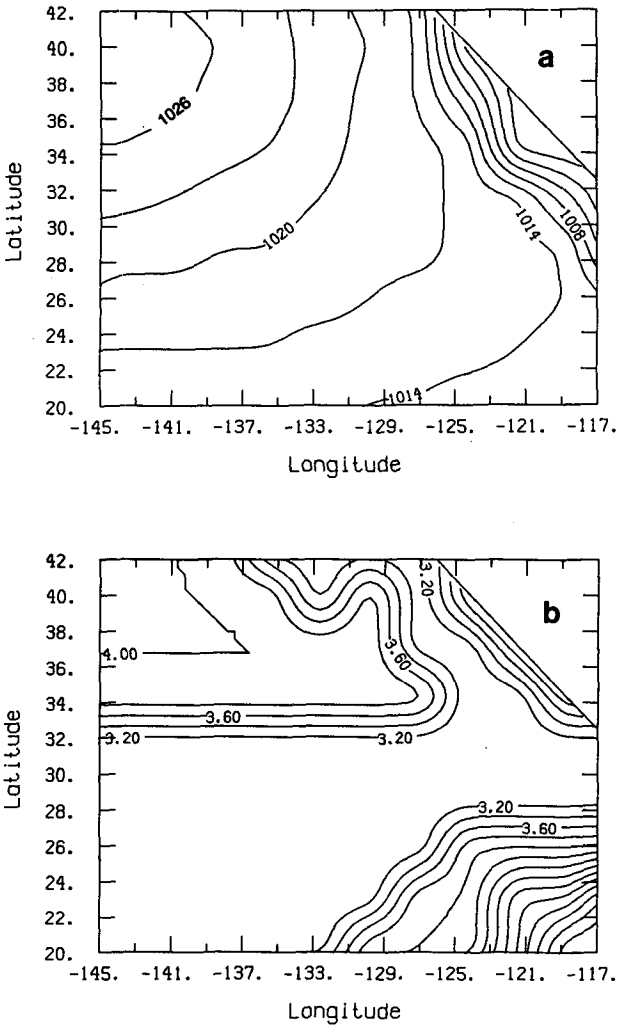

FIG. 3. (a) Mean surface pressure during FIRE period. (b) Mean water vapor mixing ratio (g kg^{-1}) at 700 mb from the ECMWF analyses.

scale divergence (Fig. 5b) is calculated from the large-scale subsidence at 850 mb and 1000 mb from ECMWF analyses using the continuity equation:

$$D_r = -\frac{\omega_{850} - \omega_{1000}}{15 \times 10^3}. \qquad (18)$$

The divergence field has two local maxima near the coast line and the eastern border and is very weak along the western border. Compared with that derived from climate data in Wakefield and Schubert (1981), the ECMWF divergence field is relatively weak along the western boundary and strong near the coastline. For convenience, the divergence field shown in Fig. 5b is designated as the reference divergence D_r.

During the observation period of FIRE, numerous drizzle showers were observed. Miller (1990, personal communication) found that although the instantaneous drizzle rate may be as high as 5 mm day^{-1}, the leg-averaged drizzle rate is at least one order smaller than this value due to a sparse distribution of drizzle. Wang and Albrecht (1992) showed the evidence that the precipitation process indeed decouples the cloud layer from the subcloud layer. Paluch and Lenchow (1991) also discussed the decoupling effect of drizzle using observational data from FIRE. They suggested that the precipitation process may create conditional instability in the boundary layer; thus, a field of stratiform clouds may be transformed into a field of shallow cumulus clouds. Wang (1993) used the one-dimensional version of the model to demonstrate the influence of drizzle on clouds and boundary-layer structure. To include effects of drizzle on the boundary-layer

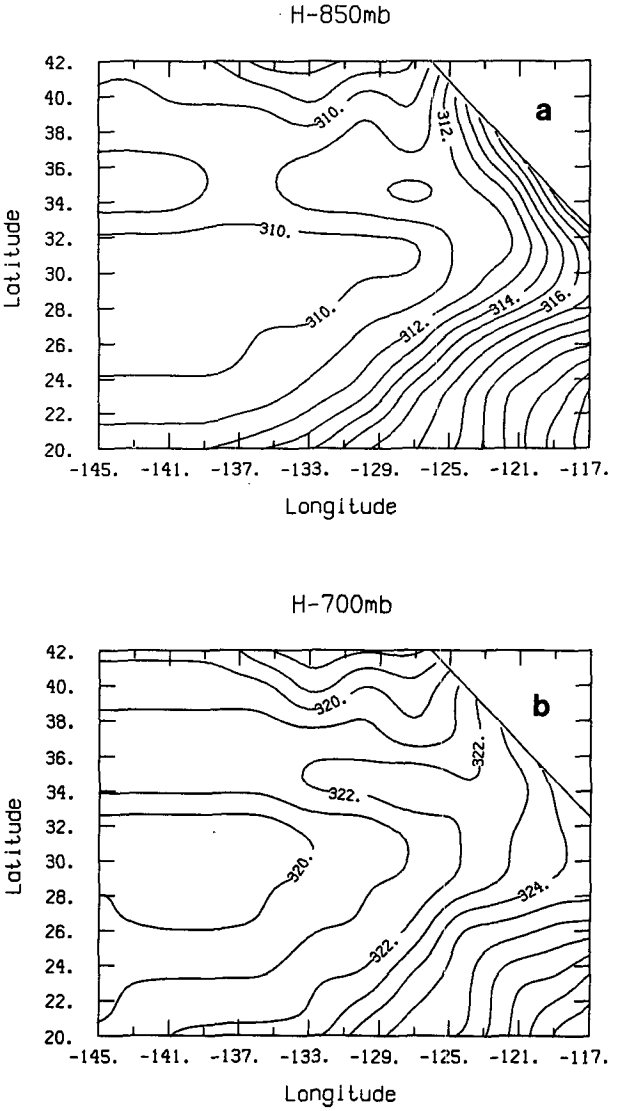

FIG. 4. Mean moist static energy fields (kJ kg^{-1}) at (a) 850 mb and (b) 700 mb derived from the ECMWF analyses.

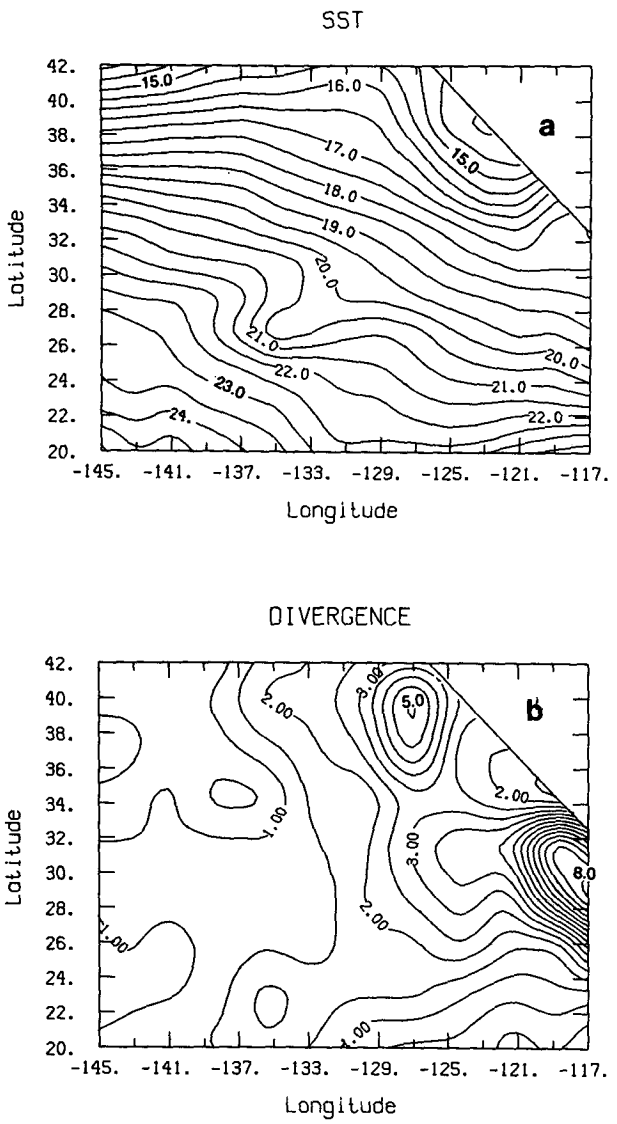

FIG. 5. (a) July mean sea surface temperature in °C from COADS; (b) large-scale divergence field ($\times 10^{-6}$ s^{-1}) calculated from large-scale velocities from the ECMWF analyses.

clouds, we specified the drizzle production efficiency constant c_0 as 10^{-3} (m^{-1}).

Although the diurnal variation is a very important component of the physical processes in the marine boundary layer, no attempt is made here to simulate this process. Instead, we simply choose a daily average value for the cosine of zenith angle:

$$\mu = 0.32 \cos(\phi) \cos(20.5°) + \sin(\phi) \sin(20.5°), \quad (19)$$

where ϕ is latitude.

4. Numerical method

The grid size is 0.4° × 0.4° latitude–longitude for the model. The temporal differencing scheme uses a common leapfrog method. Spatial differencing of the advection term uses a centered difference scheme. To remove any tendency toward decoupling the odd and even time steps, the time filter proposed by Asselin (1972) is used. The horizontal diffusion coefficient K is specified as 10^5 (m^2 s^{-1}). The smoothing effects due to horizontal diffusion are local and small, and thus should not impact the overall simulations. For the regional model, lateral boundary conditions are required for the prognostic variables. The simple lateral boundary condition applied is: the horizontal gradients of variables normal to the boundary are zero except for the coastline where the derivatives along longitudes are zero. All results presented below are steady-state solutions after 200 hours of integration of the model with a time step of 10 minutes.

5. A steady-state solution

To initialize the model, we obtain steady-state solutions from the one-dimensional version of the model with 14° and 23°C SSTs. We then interpolate boundary-layer structure based on these solutions for SST values over the entire domain. The results shown here are not sensitive to the initialization procedure. In this section we will present a steady-state solution obtained with the large-scale conditions defined in the last section. We refer to this simulation as control experiment (CNTRL). In addition, we will discuss the balance among the different processes in the boundary-layer height and cloud-layer moisture budget for the large-scale conditions specified in section 3.

a. Mean fields

The results obtained with the model represent the mean MBL structure forced by average large-scale conditions. This mean structure may, however, differ from the time-averaged structure over the period, especially when the variability in the structure is relatively large. Thus, care should be taken when comparing model results with average observations. Although moist static energy is a predicted variable in the model, liquid water potential temperature, $\overline{\theta_L}$, will be used to present the results because it is more representative of the temperature structure in the MBL.

The total water mixing ratio ($\overline{q_M}$) and liquid water potential temperature energy (θ_{L_M}) in the subcloud layer are shown in Fig. 6. The contours of both quantities closely parallel the SST and indicate a southward increase along downstream trajectories. The overall patterns of $\overline{q_M}$ and θ_{L_M} are similar to those of Wakefield and Schubert (1981) (their Fig. 9), although their simulated boundary layer is generally more moist and warmer. Two local maxima in $\overline{q_M}$ are present near the coast and the northwest corner of the domain and correspond to minima in the cloud-base heights (Fig. 7a). These features, however, may not be realistic. The

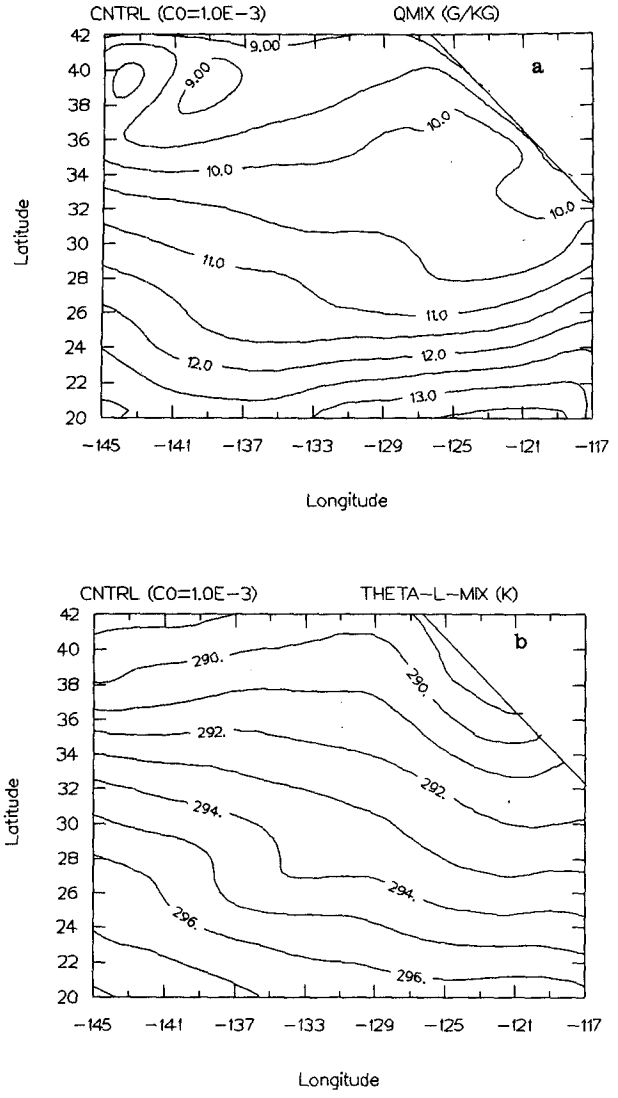

FIG. 6. (a) The simulated water vapor mixing ratio (g kg^{-1}), q_M, in the subcloud layer, and (b) liquid water potential temperature (K), θ_{LM}, in the subcloud layer.

cloud-base heights near the coast are about 50 m. This indicates that, in reality, fog may form over the low SST area with the cloud base approaching the surface, that is, $z_c = 0$. However, in the model z_c cannot be zero since it appears in the denominator in (2) and (3). Thus, with significant decreases in z_c, the model must increase $\overline{q_M}$. In addition, the low SST in these areas and the warm advection toward the low SST near the coast may result in a stable boundary layer that cannot be simulated by the model. Therefore, the model's inability of dealing with fog and stable boundary layers clearly is a weakness.

Away from cold ocean surfaces near the coast, as shown in Fig. 7a, cloud-base height rises to the southwest, in accordance with the warmer and more moist subcloud layer associated with increasing SST. The relative minimum at 28°N, 135°W is due to the low SST there. The cloud-top height shown in Fig. 7b is strongly related to the large-scale divergence. The divergence maximum near the eastern border leads to a shallow boundary layer ($z_i \approx 600$ m). Cloud-top heights increase rapidly to the west and reach 2.0 km at the southwest corner of the domain, where the large-scale divergence is only about 10^{-6} s^{-1}. This increase is also due to an increase in SST along that direction, which results in an intensified cloud-top entrainment. Consequently the horizontal gradient of z_i along trajectories is greater than that of z_c, especially in the southwest, so that the cloud layer thickens from the east to the west. This is consistent with Wakefield and Schubert (1981).

The MBL may become decoupled if drizzle or solar warming are present (Nicholls 1984). The magnitude of the discontinuities in total water, q, ($\Delta_B\bar{q} = \overline{q_B} - \overline{q_M}$), and virtual potential temperature, θ_v, ($\Delta_B\theta_v = \theta_{v_B} - \theta_{v_M}$), at the cloud-base level in the model reflects the influences of decoupling processes. Figure 8 shows $\Delta_B\bar{q}$ and $\Delta_B\bar{s}_l$ from the simulation. In general, the magnitudes of these jumps increase toward the southwest, since drizzle and entrainment intensify (presented later) along that direction. This is consistent with general observations that the cloud and subcloud layer become decoupled in the transition from the stratocumulus to trade-wind cumulus boundary layer. These jumps have their local maxima to the northwest and near the coast where surface fluxes (Fig. 9) are a minimum due to weak surface wind and low SST. These weak fluxes contribute to the decoupling over these two areas. This decoupling limits moisture transport to the cloud layer, and thus contributes to the local maxima of q_M in these two areas. We mentioned previously that the simulated boundary-layer structure may not adequately represent the time-averaged structure over this period, since the large-scale conditions provided are averaged and steady state. A good example for this case is the structure over the northwest corner. Here the averaged subtropical high is located in this area; the simulated surface fluxes are close to zero, mainly due to weak surface wind. However, it is not likely that the location of the subtropical high is completely steady state during this period. Thus, if time-dependent large-scale conditions are used, the mean structure at the northwest corner may differ from the results shown here.

The surface fluxes are strongly coupled to the SST field as shown in Fig. 9. Over the low SST areas near the coast and the northwestern corner, the fluxes are very weak as mentioned previously. They increase with SST along the downstream flow. The local minima in the fluxes at 27°N, 134°W are also related to the local minimum in SST there. The surface moisture flux reaches a maximum of 170 W m^{-2} at the southwest corner, but is less than 10 W m^{-2} close to the coast. The buoyancy flux is positive over most part of the

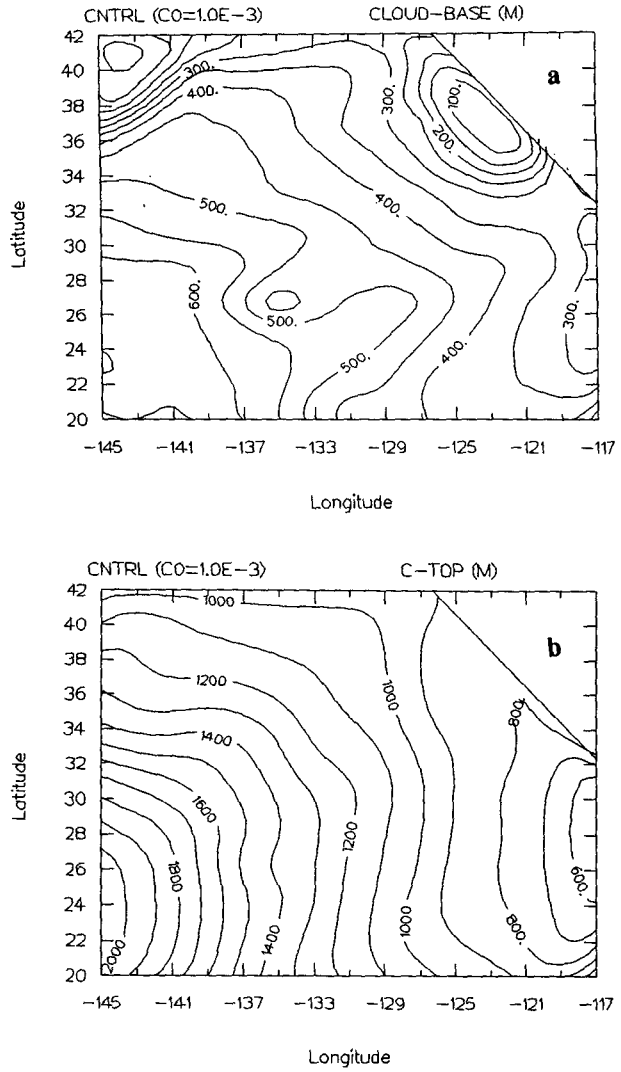

FIG. 7. (a) The simulated cloud-base heights (m) and (b) cloud-top heights (m).

domain except near the coast and the northwestern corner, where it is marginally negative. In general, the moisture flux is smaller, and the buoyancy flux is greater than those simulated in the Wakefield and Schubert (1981).

The vertical gradients of $\bar{q}$ and $\overline{\theta_L}$ in the cloud layer, γ_q and γ_{θ_L}, presented in Fig. 10 clearly show that the MBL becomes more stratified from the northeast to the southwest. The moisture gradient, γ_q, along the coast and the northern border of the domain increases considerably southward. Over these areas, weak surface fluxes due to low SST cannot balance the effects of drizzle and solar warming; thus, the strong gradients are present.

Figure 11 presents q, θ_L, and mean relative humidity (RH_T) at the top of the boundary layer. The moisture at the top increases toward the southeast due to increases of the moisture and moist static energy above clouds (Figs. 3 and 4) along that direction. The relative high value of moist static energy in the southeast results in a weak cloud-top entrainment (shown later). Since the boundary layer thickens along trajectories toward the southwest, θ_L increases along this direction.

The simulated cloud cover is shown in Fig. 12a. The cloud cover is close to unity over low SST areas along the northern border and the coast. A minimum of 0.53 at the northwest corner is related to the weak surface flux there. Another local minimum of 0.6 is located just south of the coast. The cloud cover decreases southward and reaches 0.5 in the southwest. This cloud cover pattern is closely related to the fields of large-scale divergence, drizzle, and entrainment. Divergence increases from the west to the east and reaches the

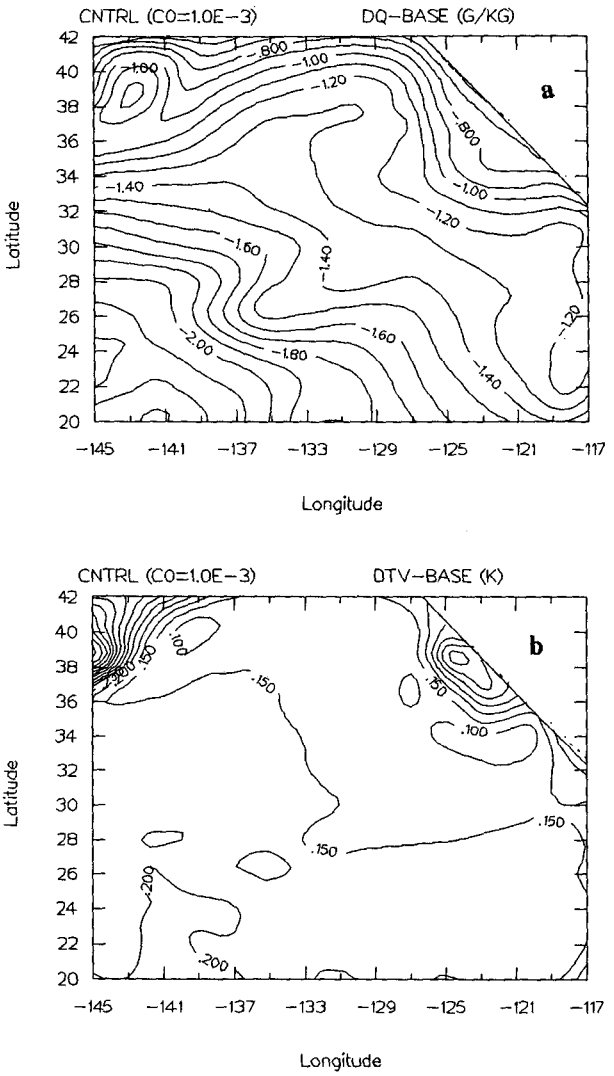

FIG. 8. (a) The simulated jumps in q (g kg^{-1}) across the cloud-base transition layer and (b) the jumps in θ_v (K) across the cloud-base transition layer.

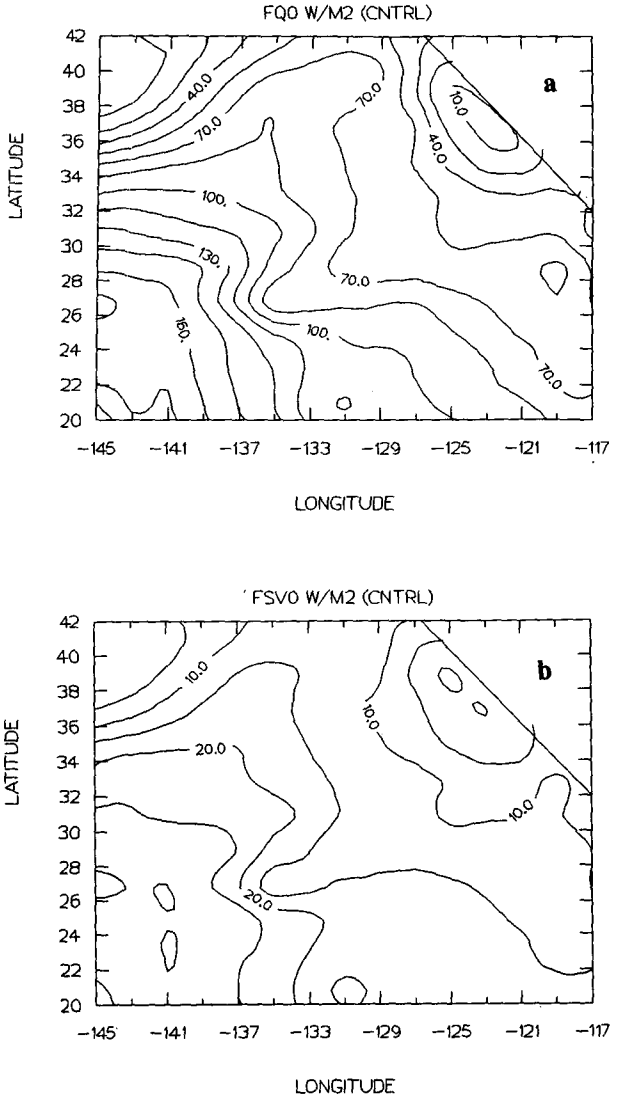

FIG. 9. The simulated surface fluxes (W m^{-2}) of (a) latent heat flux and (b) virtual dry static energy.

maximum near the eastern border. Since an increase in large-scale subsidence will decrease cloud-top heights and the relative humidity at the top of the cloud layer, the divergence field (Fig. 5b) tends to substantially decrease cloud cover in the east part of the domain. However, the drizzle rate (Fig. 12b) increases to the southwest from the coastline and reaches a maximum of 1.2 mm day^{-1} at the southwest corner. The entrainment velocity also increases toward the southwest due to the increase of SST. Thus, drizzle and entrainment tend to reduce cloud cover toward the southwest. Therefore, all these processes have contributed to this simulated cloud cover pattern. The cloudiness pattern is also seen similar to the relative humidity pattern in Fig. 11c because of the strong dependence of the cloudiness parameterization of (15) on the mean relative humidity of the cloud layer.

The drizzle rate (Fig. 12b) at the surface in the FIRE area is only 0.05 mm day^{-1} and the evaporation rate is about 0.01 mm day^{-1}. This drizzle rate is considerably less than the instantaneous drizzle rate (5 mm day^{-1}) and the leg-averaged drizzle rate (0.5 mm day^{-1}) (Miller 1990, personal communication) observed during flight 2 of FIRE. In general, the simulated evaporation rate is only ¼ of the drizzle rate. Unfortunately, we cannot determine to what extent this mean drizzle distribution is realistic since no data are available for most of the region.

Mean low cloud-top heights and low cloud cover for the FIRE IFO (1–19 July 1987) were derived on a 2.5° × 2.5° latitude–longitude grid using a 3-hourly GOES West 8-km resolution visible and infrared dataset and the analysis procedures described by Minnis et al. (1987) and Minnis et al. (1992). The results are shown

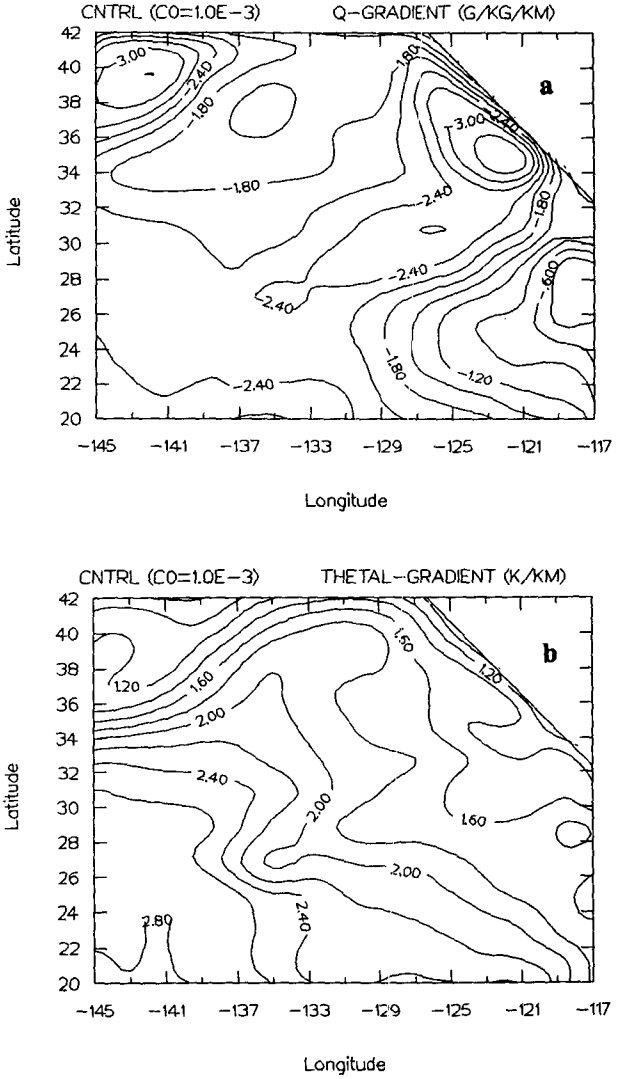

FIG. 10. The simulated gradients in the cloud layer: (a) q gradients (g kg^{-1} km^{-1}), (b) θ_L gradients (K km^{-1}).

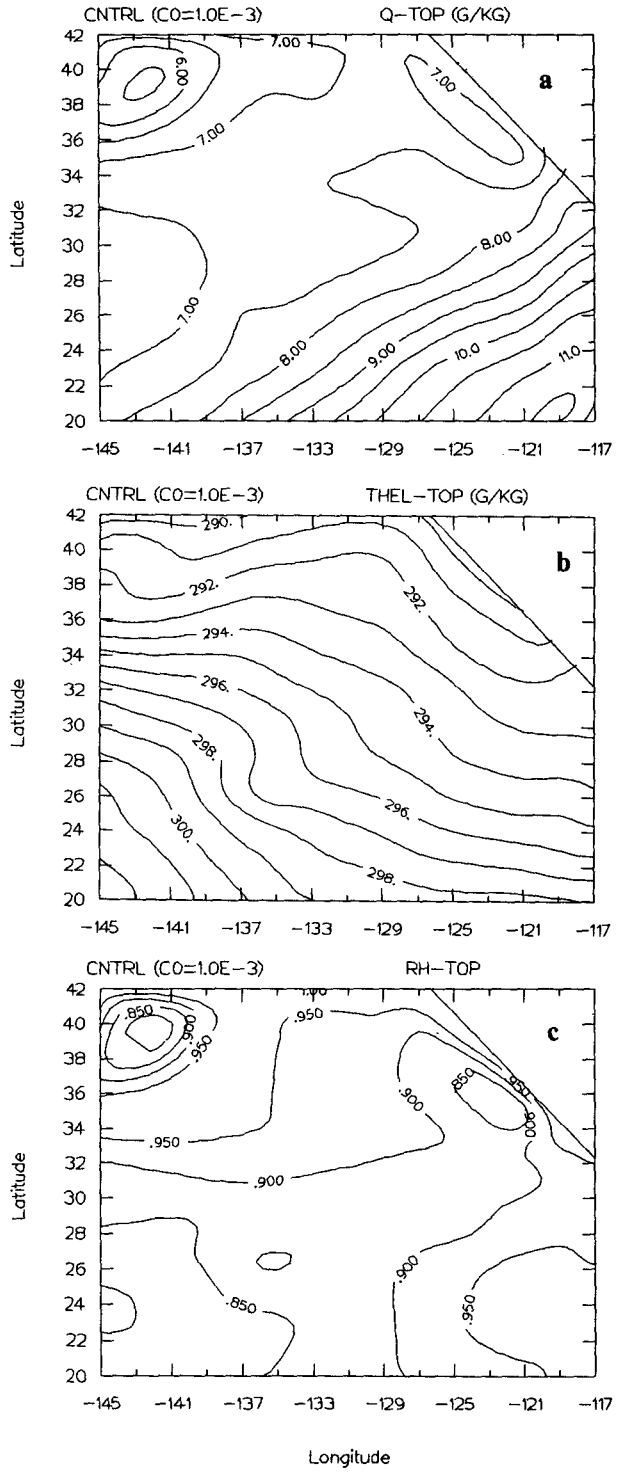

FIG. 11. (a) The simulated q (g kg^{-1}), (b) θ_L at the top of boundary layer, and (c) the mean relative humidity at the top of the boundary layer.

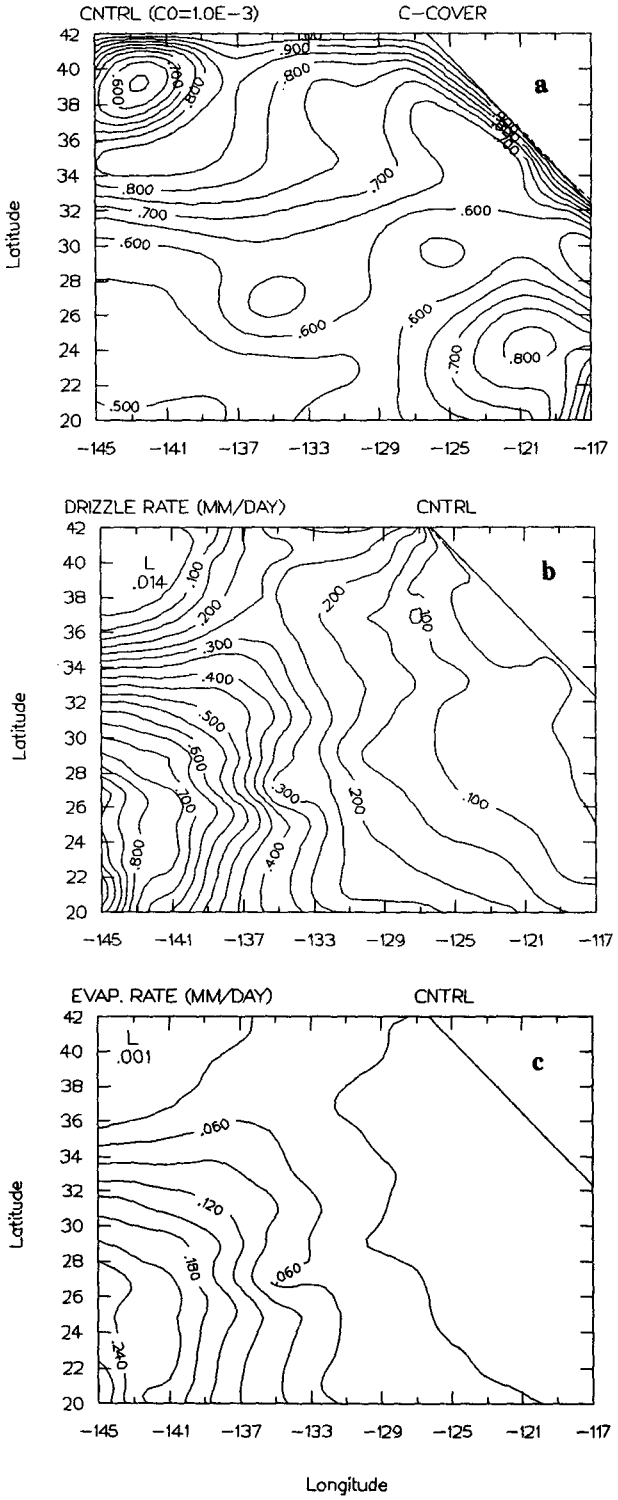

FIG. 12. (a) The simulated cloud cover, (b) drizzle rate (mm day^{-1}), and (c) evaporation rate (mm day^{-1}).

in Fig. 13, where the values over land are ignored. The satellite-derived FIRE IFO cloud heights and coverage generally follow the same patterns observed in the 1983–1987 means presented by Heck et al. (1990), although they are not as smooth because of the shorter averaging period. The FIRE IFO mean cloud cover is slightly higher and the mean low cloud heights are somewhat less than their respective 6-year average (Minnis et al. 1991). The mean satellite-derived cloud-top heights near the coast are found to be 53 m lower than the surface-based sodar measurements of the inversion base during the FIRE IFO (Minnis et al. 1992). Mean cloud cover is within ±0.03 of those derived from two surface instruments near the coast during the same time period. The large-scale, 6-year mean (1983–88) cloud cover patterns are very similar to those derived from COADS ship data, with mean satellite cloudiness being 0.05 lower than the COADS observations (Minnis et al. 1991). Such differences may be attributed to differences in viewing conditions. The large-scale 5-year mean cloud-top heights are very similar in magnitude and spatial variation to the Nieburger (1961) July inversion base data (see Heck et al. 1990). Thus, it is concluded that the results in Fig. 13 represent a relatively accurate depiction of the cloud fields for this area and time period.

The basic patterns of both simulated and satellite-derived cloud-top heights are qualitatively consistent. Both have relatively low values near the coast and the eastern border and increase toward the southwest. Both the simulated and satellite derived cloud-top heights are about 800 m near the coast. Along the eastern border, the model predicts only 500 m for the cloud-top height compared with 1000 m derived from satellite data. In the northwestern part of the domain, the satellite-derived heights are about 1350 m compared with 1000 m from the simulation. At the southwest corner, the simulated value reaches 2000 m, 350 meters higher than the satellite derived.

The simulated (Fig. 12a) and satellite-derived (Fig. 13b) cloud cover also show some qualitative similarity. A relative minimum is seen in the northwest of both domains, although the satellite-derived minimum extends farther to the east. The satellite-derived cloud amounts reach the maximum of 0.9 at 36°N, 138°W, corresponding to 0.85 in the simulated results. The model, however, extends the 0.9 contour to the California coast where the satellite-derived cloudiness drops to 0.6. Both fields have relative maxima in the southeast part of the domain. The simulated local maximum, though, is smaller and 5° east of the satellite-derived peak. The observed cloud cover diminishes to 0.4 in the southwest corner of the domain where the simulated value remains above 0.5. The domain average from the simulation is 0.67 compared with 0.74 of that derived from satellite data. The satellite-derived cloud amount has a relatively high value in the center part of the domain, and decreases toward the coast and the

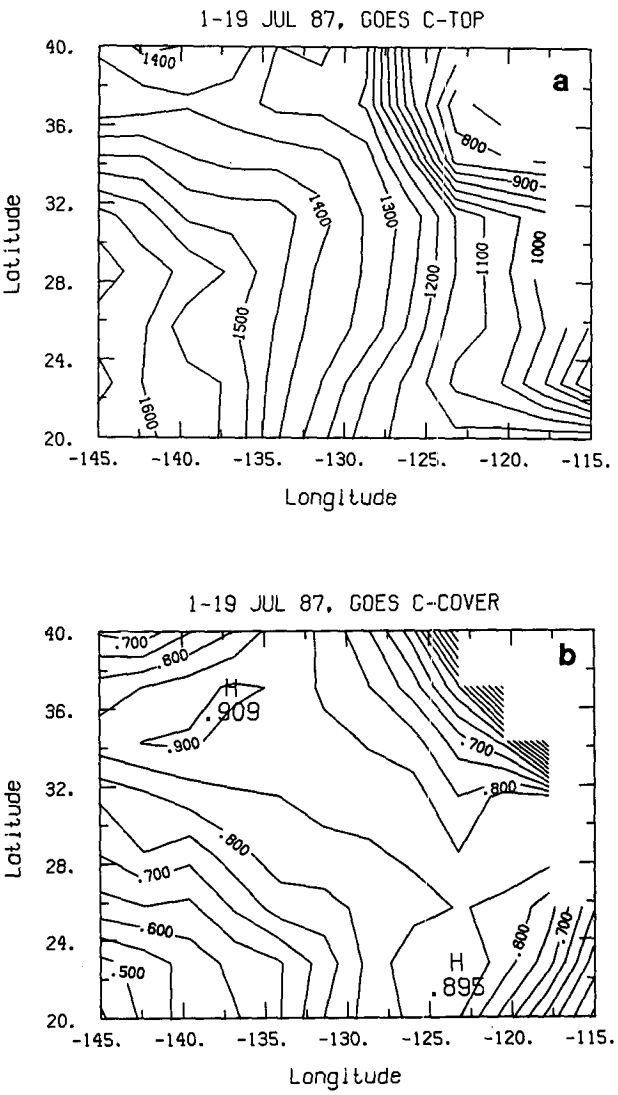

FIG. 13. Mean cloud properties derived from GOES for 1–19 July 1987. (a) Mean cloud-top heights (m); (b) mean low cloud cover.

southeast. The simulated cloud cover reaches maximum (0.9) close to the coast and decreases to the center and does not show significant decreases toward the southwest.

Differences between the two cloud cover fields may arise from a number of sources. The simulation may not capture fluctuations in cloudiness due to variable large-scale conditions. For example, near the coast, the low-level winds occasionally blow from land resulting in extensive clearing of the marine stratus (Kloesel 1991) for several days. The average surface wind (Fig. 2) has no offshore component so no clearing is produced along the coast. The model also does not include a diurnal cycle even though the diurnal variability in marine stratocumulus cloud coverage and altitude is substantial (e.g., Minnis and Harrison 1984; Heck et

al. 1990; Minnis et al. 1992). Consequently, inclusion of a stable boundary-layer parameterization and diurnal variations in the model is likely to significantly reduce the cloud cover near the coast.

The absence of the 29 and 30 June data in the satellite cloudiness could affect the mean values to some extent. Examination of the imagery suggests that the coastal area was overcast during both days. Thus, the coastal means would be about 4% greater than those given, not enough to account for the differences. The satellite-derived mean cloudiness calculated for 1–31 July is very similar to the 19-day averages in Fig. 13b. Thus, it is unlikely that the basic patterns in Fig. 13b would change considerably if the missing days were included.

Errors in the large-scale conditions may be another source for the simulated versus observed cloud cover and cloud-top height differences. The marine part of the domain is practically devoid of standard meteorological observations. Thus, the ECMWF and other global analyses must rely on satellite observations, climatology, and other nonconventional sources to initialize the state fields in this and other areas. The accuracy of these inputs is unknown. Given the comparison of the FIRE 850-mb moisture with its ECMWF counterpart and moisture in this area (e.g., Minnis et al. 1992), it is likely that the potential errors in the large-scale conditions for this model are significant. The sensitivity to some of these errors is explored in a later section.

b. *Budgets of z_i and q*

From (1)–(7), it is clear that the local equilibrium structure of the MBL is determined by a balance among the large-scale horizontal advection, subsidence, turbulent flux divergence, horizontal mixing, and precipitation (for total water mixing ratio) or radiation (for moist static energy). Although one-dimensional models can be used to study the equilibrium structure (e.g., Betts and Ridgway 1989), horizontal advection may play an important role in the balance. Schubert et al. (1979) used a downstream simulation and analytical solution to show that the adjustment time for cloud top is relatively long, and thus the boundary-layer depth may be far from its horizontally homogeneous steady-state value.

Here we try to evaluate the relative importance of the different processes in budgets. Only the budgets of cloud-top height and cloud-layer moisture are presented. The budget for cloud-top height is given by (7). The budget equation for the averaged total water mixing ratio in the cloud layer ($\overline{q_A}$) can be written as

$$\frac{\partial \overline{q_A}}{\partial t} = -\gamma_q \overline{w_A} - \frac{\overline{w_i' q_i'} - \overline{w' q_B'}}{\Delta z_c} + \gamma_q \frac{dz_A}{dt} - \nu \cdot \overline{\nabla q_A} + K \nabla^2 \overline{q_A} + P_A. \quad (20)$$

The first term on the right-hand side is vertical advection due to large-scale subsidence, the second term is the flux divergence term, the third term is vertical advection due to changes of the mean cloud-layer height, the fourth term is horizontal advection, the fifth term is horizontal diffusion, and the last term is drizzle. We will present the horizontal distribution of each term in (7) and (10) and discuss its importance in each budget.

Figure 14 shows the fields of large-scale subsidence, cloud-top entrainment, and horizontal advection in the z_i budget [Eq. (7)]. The tendency and diffusion terms (not shown here) are generally one order smaller in magnitude than the other terms. Thus, the equilibrium boundary-layer height is basically determined by a balance among subsidence, entrainment, and horizontal advection. The subsidence shown in Fig. 14a is directly proportional to the large-scale divergence (Fig. 5b). Strong subsidence substantially limits z_i along the eastern border of the domain where the local subsidence maxima (-4.5 mm^{-1}) balances both entrainment (1.5 mm s^{-1} in Fig. 14b) and positive advection (2.0 mm s^{-1} in Fig. 14c). The entrainment velocity increases from the northeast to the southwest due to a stronger surface buoyancy flux and reaches a maximum of 7 mm s^{-1} at the southwest corner of the domain. The weak entrainment (less than 1.5 mm s^{-1}) over the northwest and along the coast is related to the weak surface buoyancy fluxes. For the most of the domain, it is entrainment that balances both subsidence and negative advection. When subsidence is weak, advection may play a larger role in the balance. For example, at 26°N, 141°W subsidence is approximately -1 mm s^{-1}, entrainment velocity is 7 mm s^{-1}, and advection is -5.5 mm s^{-1}. In this region, gradients of z_i are strong and approximately parallel to the wind vectors, and thus there is a negative maxima of advection. In the southeast area, where subsidence is only marginally negative, entrainment (2 mm s^{-1}) is almost entirely balanced by the negative advection (-2.5 mm s^{-1}). Consequently, advection balances most of the entrainment for these two areas.

As was the case for z_i budget, the tendency and diffusion terms (not shown here) in the moisture budget [Eq. (10)] are generally very small compared with the other terms. Subsidence dries the cloud layer since large-scale vertical motion advects drier air downward in the boundary layer (Fig. 15a). This large-scale vertical advection is greatest (-0.6 g kg^{-1} day^{-1}) when the large-scale subsidence and q gradient of the cloud layer obtain their large values at 30°N, 123°W. The moisture flux divergence term moistens the cloud layer for the entire domain and is the largest term in the balance (Fig. 15b). The magnitude of this term is relatively small along the northern border and the coast due to the low SSTs. It increases from the northeast to southwest due to intensified convection. This term, however, has a maximum of 2.4 g kg^{-1} day^{-1} at the

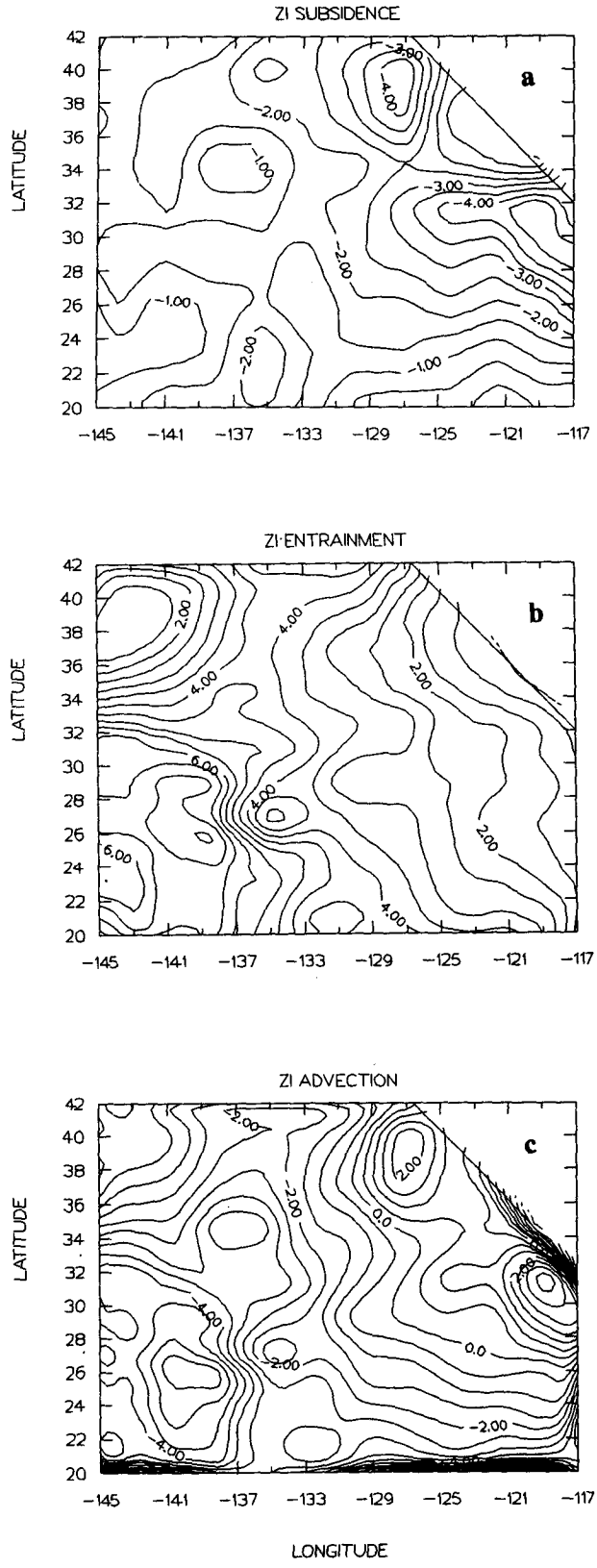

FIG. 14. Terms in the z_i budget (mm s^{-1}). (a) Subsidence; (b) entrainment velocity; (c) horizontal advection.

eastern border because the cloud-layer thickness is limited by the strong subsidence there. Changes in the cloud layer moisture due to changes in the height of the mean cloud-layer level are shown in Fig. 15c. This term is essentially related to the horizontal advection of the mean cloud-layer level for a steady-state solution. For a cloud layer with a negative moisture gradient, the negative tendency of the mean cloud-layer level tends to dry it. Thus, this term tends to dry the cloud layer by increasing the mean cloud-layer level along trajectories. Figure 15d shows that the horizontal advection is negative for most of the area. The magnitude of the drying due to horizontal advection is similar to that of vertical advection by subsidence for much of the area. Near the eastern border of the domain, however, the negative maximum of horizontal advection (-2.2 g kg^{-1} day^{-1}) almost balances all the moistening due to the turbulent flux divergence (2.4 g kg^{-1} day^{-1}). The drizzle flux term shown in Fig. 15e is consistent with the general pattern of the drizzle rate field in Fig. 12b. The value of the drizzle term is small (0.1 g kg^{-1} day^{-1}) near the coast at the northwest corner. It increases toward southwest from the coast with thickening of the cloud layer. The drizzle contribution is generally more than 20% of that of the flux divergence term. Over cold ocean surfaces, the flux is generally small and thus the drizzle term is not negligible compared with the flux term. Thus, a small amount of drizzle may still have important influences on the MBL structure over cold sea surfaces if surface fluxes are weak. In the next subsection, we will show that simulated cloud cover is sensitive to the specification of drizzle. This budget study indicates that horizontal advection has a strong impact on both MBL heights and equilibrium thermodynamic structures in the MBL. Consequently advection should be accounted for in the validation of equilibrium structures of a one-dimensional model.

6. Sensitivity experiments

The large-scale conditions used in this study are subject to uncertainties due to a lack of observations over oceans in the ECMWF analyses. In particular, we specified the specific humidity at 850 mb the same as that at 700 mb since the moisture at 850 mb from ECMWF analyses is considerably higher than that observed during FIRE. Although the prediction of vertical velocities over subtropics is better than that in the deep tropics, a slight uncertainty of this variable may still lead to a significant difference in the prediction of low-level cloudiness based on some one-dimensional model results (Brill and Albrecht 1982; etc.). To assess the sensitivity of the model results to these uncertainties, we perform two model runs: one with an addition of 2×10^{-6} s^{-1} to the large-scale divergence field in the experiment CNTRL (DIV), and another with an addition of 2 g kg^{-1} to the specific humidity at 850 mb in the experiment CNTRL (MOI).

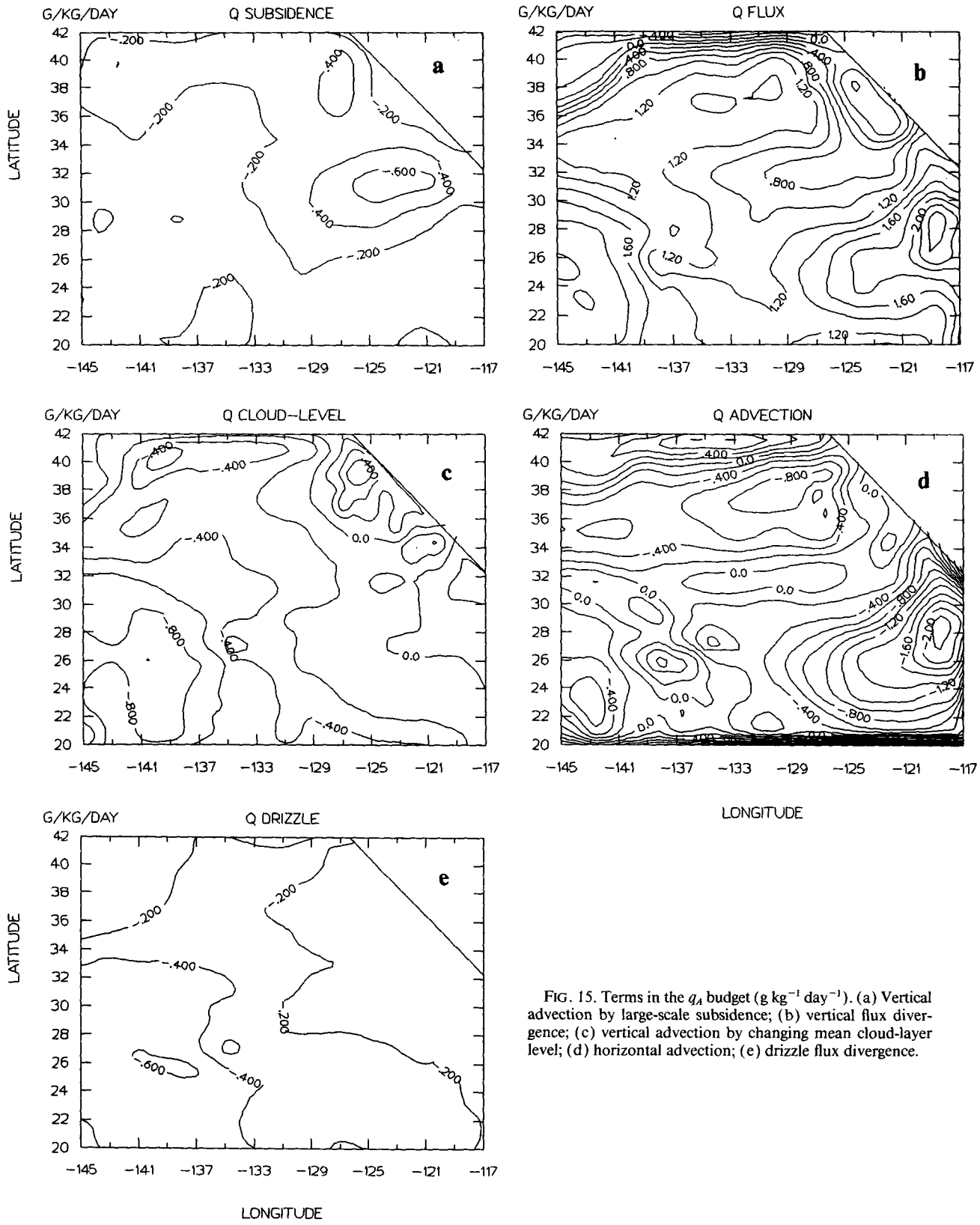

FIG. 15. Terms in the q_A budget (g kg^{-1} day^{-1}). (a) Vertical advection by large-scale subsidence; (b) vertical flux divergence; (c) vertical advection by changing mean cloud-layer level; (d) horizontal advection; (e) drizzle flux divergence.

Effects of shortwave radiation and precipitation on the structure of the marine boundary layer have been a focus of many studies. Although the regional model uses relatively simple radiation and drizzle parameterizations, it provides a framework to study influences of shortwave radiation and drizzle on the distribution of cloud cover and boundary-layer height. To illustrate these effects, we perform another three experiments: one with deactivation of the drizzle parameterization (NDR), another with cosine of zenith angle equal to zero (NSW), and the third with both drizzle and shortwave radiation parameterization deactivated (NSD). We realize that a better way to study effects of shortwave radiation is to perform diurnal simulations with the regional model. Wang (1990) and Brill and Albrecht (1982) used the similar one-dimensional models to simulate diurnal variations of marine stratocumulus and trade-wind cumulus clouds. Using the steady-state sensitivity tests, we simply try to illustrate some effects of the shortwave radiation on the simulated cloud regime in the model. The conditions for these experiments are listed in Table 1.

TABLE 1. Conditions of sensitivity experiments.

Experiments	Conditions
CNTRL (section 5)	Divergence = D_r (Fig. 5b); q_{850} = Fig. 3b; c_0 = 10^{-3} (m^{-1}); μ = Eq. (4)
DIV	Divergence = D_r (CNTRL) + 2.0×10^{-6} (s^{-1})
MOI	q (850 mb) = q_{850} (CNTRL) + 2.0 (g kg^{-1})
NDR	c_0 = 0 (no drizzle); μ = Eq. (4)
NSW	c_0 = 10^{-3} (m^{-1}); μ = 0 (no solar radiation)
NSD	c_0 = 0; μ = 0

Figure 16 presents the results from DIV. It is seen that cloud-top height decreases due to the increase of the large-scale divergence compared with that of the experiment CNTRL. The maximum z_i at the southwest from the experiment DIV is 1500 m, 400 m lower than that from the experiment CNTRL, while it is 300 m from the experiment DIV compared with 700 m from the experiment CNTRL for the minimum at the east boundary. A significant decrease in boundary-layer height leads to a decrease in the mean relative humidity at the top of the cloud layer, as shown in Fig. 16c. Consequently, the cloud cover considerably decreases for the entire domain owing to the stronger divergence. The simulated clouds become more broken toward the northern boundary of the area. The averaged cloud cover over the entire domain drops to 0.46 from 0.7 of the experiment CNTRL as shown in Table 2. It is seen that the simulated cloud cover is sensitive to the specification of large-scale divergence. In addition, the drizzle rate becomes reduced due to decreases in the depth of the cloud layer. The average drizzle rate for the domain is 0.12 compared to 0.27 in CNTRL.

Results of experiment MOI (Fig. 17) show that an increase in the moisture above clouds slightly decreases cloud-top heights since the longwave radiative cooling at the cloud-top decreases due to an increase in downward longwave radiative flux at the cloud top as discussed in Betts and Ridgeway (1989). The cloud cover increases for the entire domain since the boundary layer becomes more moist (Fig. 17c) due to the increase in the moisture above clouds. The average cloud cover is 0.81, an increase of 0.14 from that of CNTRL.

Deactivation of the drizzle parameterization results in a slight thickening of the boundary layer and a considerable increase in the cloud cover, as shown in Fig. 18. The cloud cover pattern is significantly different from that of CNTRL. At the southwest corner, clouds are solid compared with 0.65 of cloud cover from CNTRL. The average cloud cover is increased by 0.23 from that of CNTRL. This increase in the cloud cover is mainly caused by an increase of moisture in the boundary layer (Fig. 18c) due to the suppression of drizzle as discussed in Wang (1993) and Albrecht (1993).

The role of shortwave radiation is illustrated by the comparison of the results of NSW (Fig. 19) and CNTRL. The deactivation of the shortwave radiation increases radiative cooling in the boundary layer; thus, the entrainment velocity at the cloud top increases (Fig. 19c). The maximum cloud-top height reaches 2600 m at the southwest corner and the minimum cloud-top height at the eastern border is about 700 m. Although the averaged cloud cover increases by 0.06, its pattern changes little.

Figure 20 show the results from experiment NSD. The cloud cover in the case is 1 everywhere in the domain (not shown here). The suppression of drizzle and shortwave radiation leads to a significant increase in the boundary-layer height that reaches 2800 m in the southwest. The jump of θ_v across the cloud-base stable layer and θ_L gradient of the cloud layer for this experiment is also shown in Fig. 20. Comparing these results with those from CNTRL (Figs. 8 and 10), one may see that the magnitude of the jump and the stability of the cloud layer are significantly reduced by deactivation of the drizzle and shortwave radiation processes.

One may isolate the effects of drizzle process from shortwave radiation process by comparing results from experiments NDR with NSD and those from NSW with NSD, respectively. It is seen from these comparisons that each of these processes reduces the simulated cloud cover and boundary-layer height. We should bear in mind that these results are from steady-state solutions, a simulation with diurnal variation may result in a greater sensitivity of cloudiness to shortwave radiation (Bougeault 1985).

7. Discussion

From the comparisons between the simulated and the satellite-derived results, it appears that while the

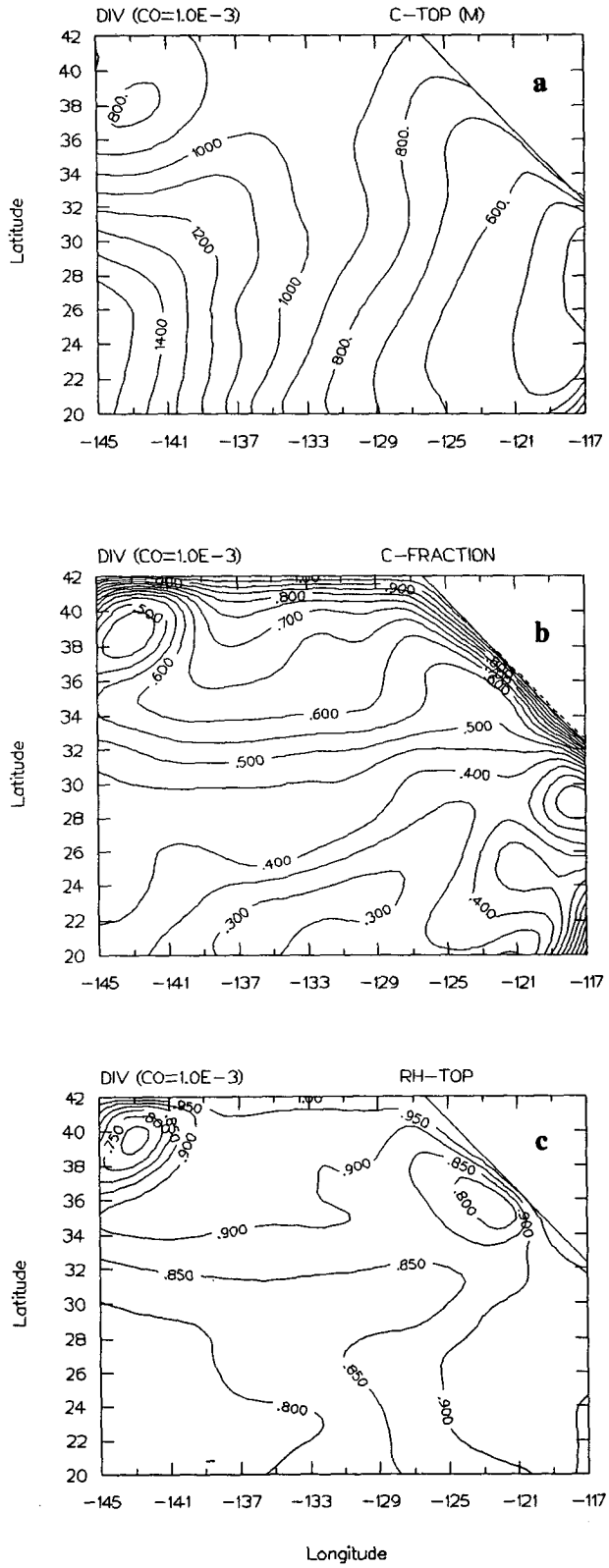

FIG. 16. Results from sensitivity experiment DIV. (a) Cloud-top heights (m); (b) cloud cover; (c) the mean relative humidity at the top of the boundary layer.

agreement between the two cloud-top height fields is reasonably good, the agreement between the two cloudiness fields is less satisfactory. As discussed in the previous sections, the overprediction of the cloudiness along the coast and the northern border of the domain is probably due to the lack of diurnal variation and off-land flow in the model. In the southwest, while the satellite-derived field has a strong gradient toward the southwest, the gradient of the simulated cloudiness in the area is significantly less. The satellite-derived cloud fraction gives 0.85 in the central area, a value significantly larger than the simulated value from the experiment CNTRL, 0.5.

The potential causes for this discrepancy are either that the simulated cloud layer is too moist or that the cloudiness parameterization does not adequately represent all important physical processes that regulate cloudiness, or both. Unfortunately, this study cannot determine what causes this apparent discrepancy because of a lack of boundary-layer data in the area. However, the contours of the satellite-derived cloudiness tend to be parallel to those of cloud-top height in the southwest. This feature may suggest that the cloudiness be correlated to cloud-top entrainment and the boundary-layer mixing, because a high cloud-top height is a result of a strong entrainment and tends to lead to a weaker mixing in the boundary layer. The simulated fields, however, show much less correlation between the cloudiness and boundary-layer height. In particular, in the experiment NSD, the resulted cloudiness is 100% for the entire domain even though the cloud tops are very high. Thus, a new dynamic parameter that explicitly represents the cloud-top versus cloud-layer mixing, for example, w_{ei}/ω^*, may be included in the cloudiness parameterization (15). Basically, the parameter, w_{ei}/ω^*, represents the relative effect of cloud-top entrainment to the cloud-layer mixing on the structure near the boundary-layer top. For example, applying (9) to the boundary-layer top, one may obtain (Wang and Albrecht 1986):

$$(\varphi_u - \varphi_d)_{z_i} = \frac{w_{ei}}{\omega_i^*}(-\Delta\overline{\varphi_i} + \text{source terms}), \quad (21)$$

where subscript d denotes environment downdraft. It is seen that a larger value of w_{ei}/ω_i^* gives a larger variability of moisture and temperature and a smaller value leads to a relatively homogeneous structure. Thus, for the same mean structure, a larger value of w_{ei}/ω_i^* may result in a smaller cloud fraction than a smaller value of w_{ei}/ω_i^*. Several authors (Deardorff 1980; Albrecht et al. 1985; Wang and Albrecht 1986) have used observations and numerical models to show that the cloud structure is closely related to this parameter. Although the above discussion is tentative, it does appear that the inclusion of this parameter in the cloudiness parameterization may improve the prediction of marine boundary-layer clouds.

TABLE 2. The results of sensitivity experiments.

	CNTRL	DIV	MOI	NDR	NSW	NSD
Averaged precipitation rate (mm day^{-1})	0.27	0.12	0.25	0.0	0.5	0.0
Averaged evaporation rate (mm day^{-1})	0.06	0.03	0.05	0.0	0.14	0.0
Averaged cloud cover	0.67	0.47	0.81	0.90	0.73	1.0

Since decoupling is one of the important features of the simulated results, a brief discussion on the decoupled structure predicted by the model is worthwhile. The simulated vertical profiles of q and θ_L at 31°N, 121°W (the aircraft soundings of FIRE were taken nearby) from experiments CNTRL and NSD are presented in Fig. 21. These profiles clearly demonstrate the stabilizing effects of both shortwave radiation and drizzle. The simulated profiles (even without shortwave radiation and drizzle) have appreciable decoupled structures. The discontinuities at the top of the mixed layer are $\Delta q \approx -0.8 - -1.3$ g kg^{-1} and $\Delta\theta_L \approx 0.2° - 0.6$°C, respectively. For comparison, the mean profiles of all soundings are also presented in Fig. 22 (Jensen 1993, personal communication). The average boundary-layer height of the mean soundings is 880 m and the average SST is 17.5°C compared with 18°C at the same location from COADS data. The simulated structure is more moist and warmer than the mean sounding. It is clearly seen that the mean profiles of the soundings do not have the strong decoupled features as shown in the simulated profiles. Thus, it is concluded that the model overpredicts decoupling in these cases. Furthermore, this overpredicted decoupled structure contributes to the overprediction of q and θ in the subcloud layer.

It should be noted that the discontinuities that occur at the cloud base are parts of the model structure that regulate the coupling between the cloud and subcloud layer in the model. They may never vanish due to the presumed model structure (Fig. 1). Thus, the model is not able to predict a complete well-mixed boundary layer. On the other hand, if these discontinuities can be minimized by the model for well-mixed conditions in the boundary layer, the difference between the model structure with small discontinuities at the cloud base and a complete well-mixed structure may be sufficiently small and can be neglected. At this point, we refer to a recent paper by Bretherton (1993). He pointed out that a weakness existed in the formulation of mass flux in the cloud layer [Eq. (12)]. He argued that the adjustment time (τ_{adj}) should be a variable instead of a constant as used in the present study. He showed that the model results (including cloudiness) are sensitive to the choice of this parameter and smaller values of this parameter result in better simulations of stratocumulus boundary layer because a larger detrainment resulting from a smaller value of τ_{adj} tends to moisten and cool the cloud layer. Thus, a new formulation of mass flux with small values of τ_{adj} for the stratocumulus cloud conditions and large values for the trade-wind cumulus cloud conditions is likely to produce a more well-mixed boundary layer than those shown in Fig. 21 as demonstrated in Wang (1993). Clearly, it is an area that needs to be improved in further studies.

8. Summary

In this study, a regional version of a two-layer model is used to simulate boundary-layer clouds over the eastern North Pacific for the period of 29 June–19 July 1987. The averaged large-scale conditions over this period needed to drive the model are derived from ECMWF analyses and COADS data.

The simulated distribution of cloud-top height and cloud cover shows some qualitative agreement with available satellite data. The budget study shows that horizontal advection may play an important role in determining equilibrium boundary-layer structures. The simulated clouds are shown to be sensitive to the specification of large-scale divergence, drizzle, and shortwave radiation. These processes tend to substantially decrease fractional cloudiness.

As discussed previously, some weaknesses of the model clearly need to be addressed in future studies. First, the inability of dealing with fog and the stable boundary layer may lead to unrealistic solutions over areas with low SST and extremely weak surface fluxes. Second, the model may overestimate decoupling between the cloud and the subcloud layer when the drizzle and shortwave radiation processes are not present. Third, a dynamic parameter that represents the cloud-top and cloud-layer mixing may be considered in the cloudiness parameterization.

Owing to its influence on the planetary albedo, changes in low-level cloudiness could contribute substantially to climate change (Randall et al. 1984). Furthermore, Slingo (1990) estimated that an accuracy of about 1% in the prediction of the absolute cloud amount is required if the effect of low clouds on climate is to be determined. Thus, the possible strong sensitivity of the MBL cloudiness to large-scale divergence and drizzle shown in this study suggests that both the large-scale flow and cloud microphysics need to be predicted or parameterized accurately to achieve this accuracy of the prediction of low-level cloudiness.

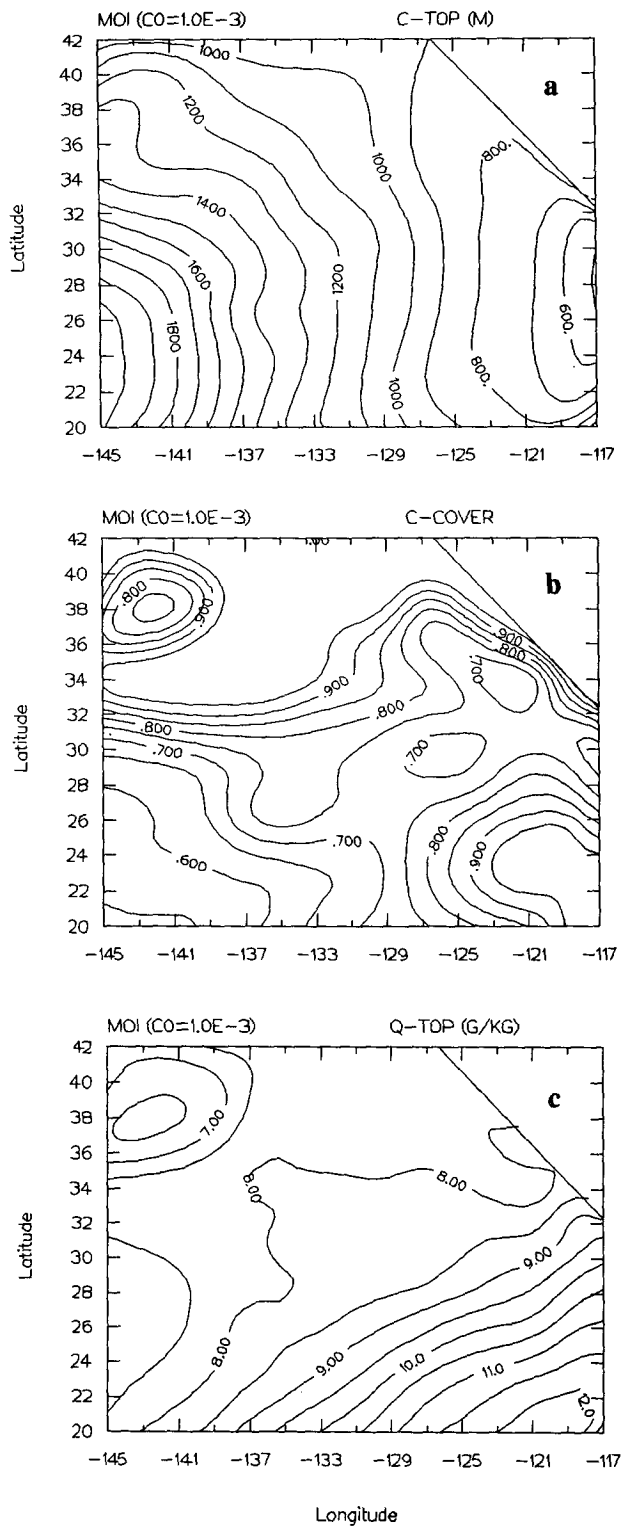

FIG. 17. Results from sensitivity experiment MOI. (a) Cloud-top heights (m); (b) cloud cover; (c) total water mixing ratio (k kg^{-1}) at the top of the boundary layer.

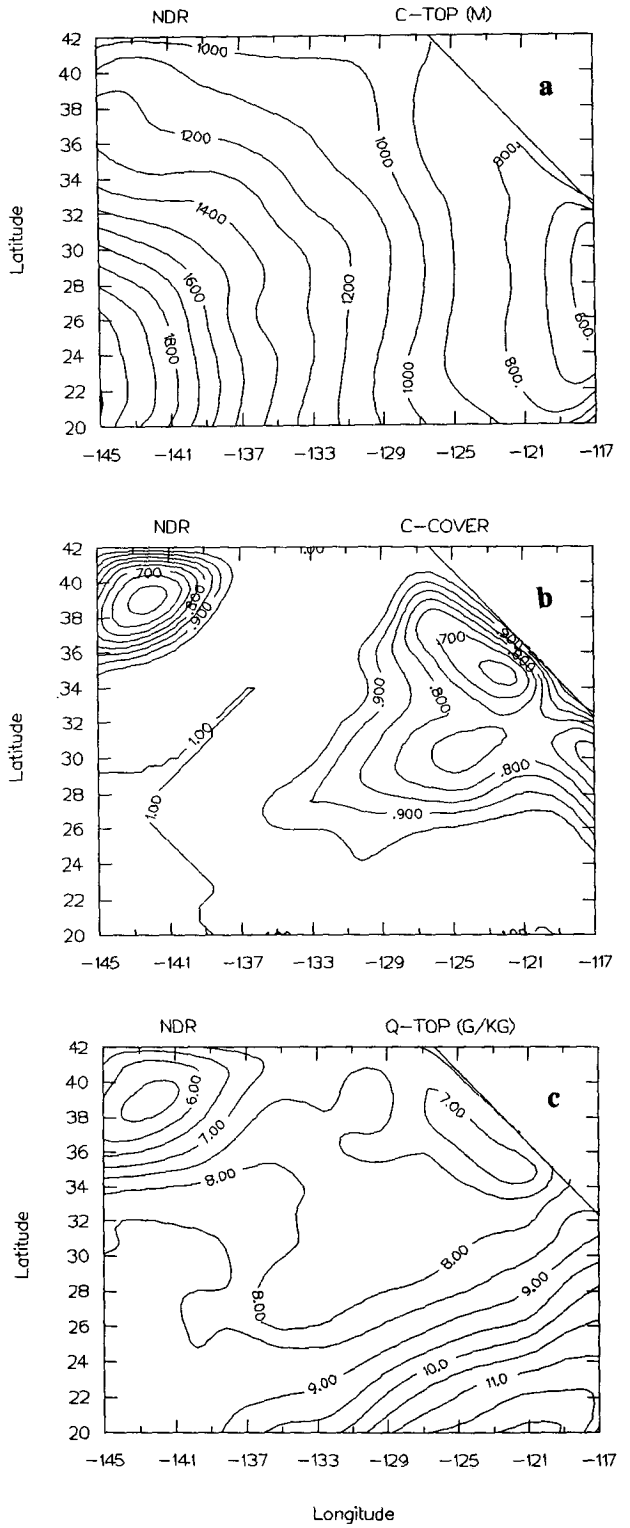

FIG. 18. Results from sensitivity experiment NDR. (a) Cloud-top heights (m); (b) cloud cover; (c) total water mixing ratio (k kg^{-1}) at the top of the boundary layer.

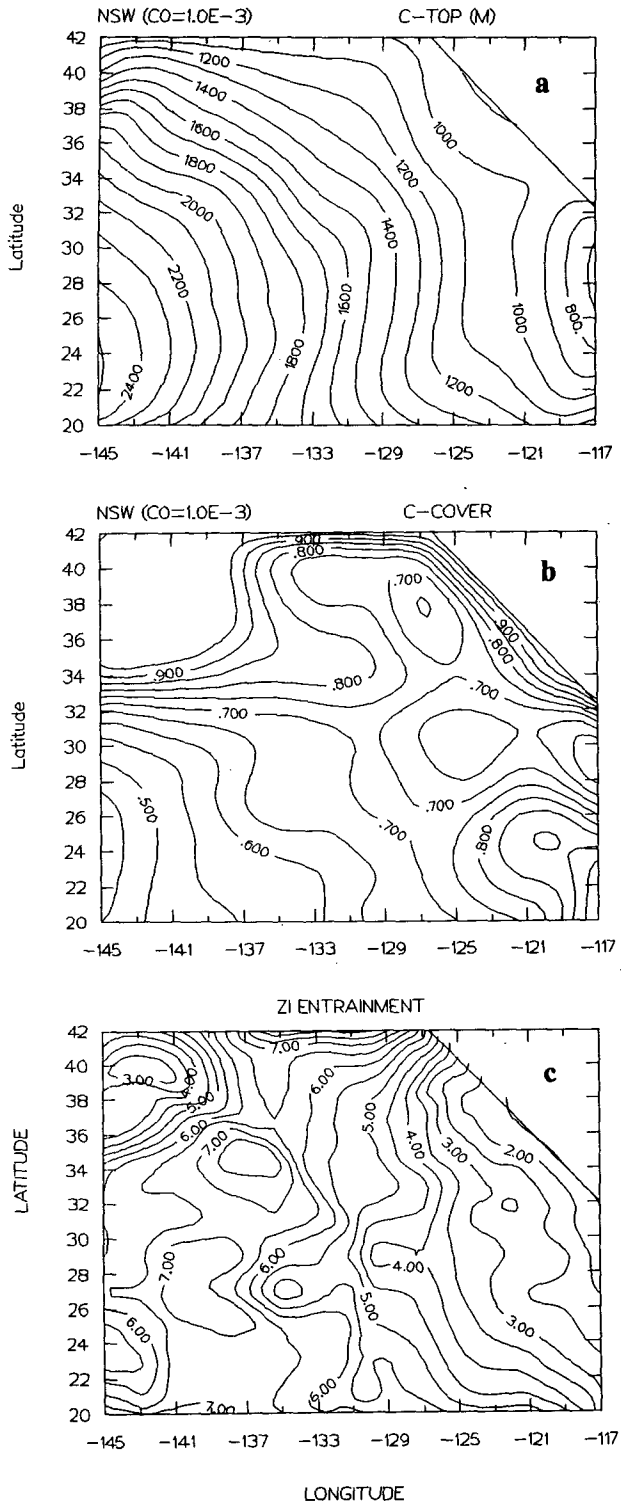

FIG. 19. Results from sensitivity experiment NSW. (a) Cloud-top heights (m); (b) cloud cover; (c) entrainment velocity at the top of the boundary layer (mm s^{-1}).

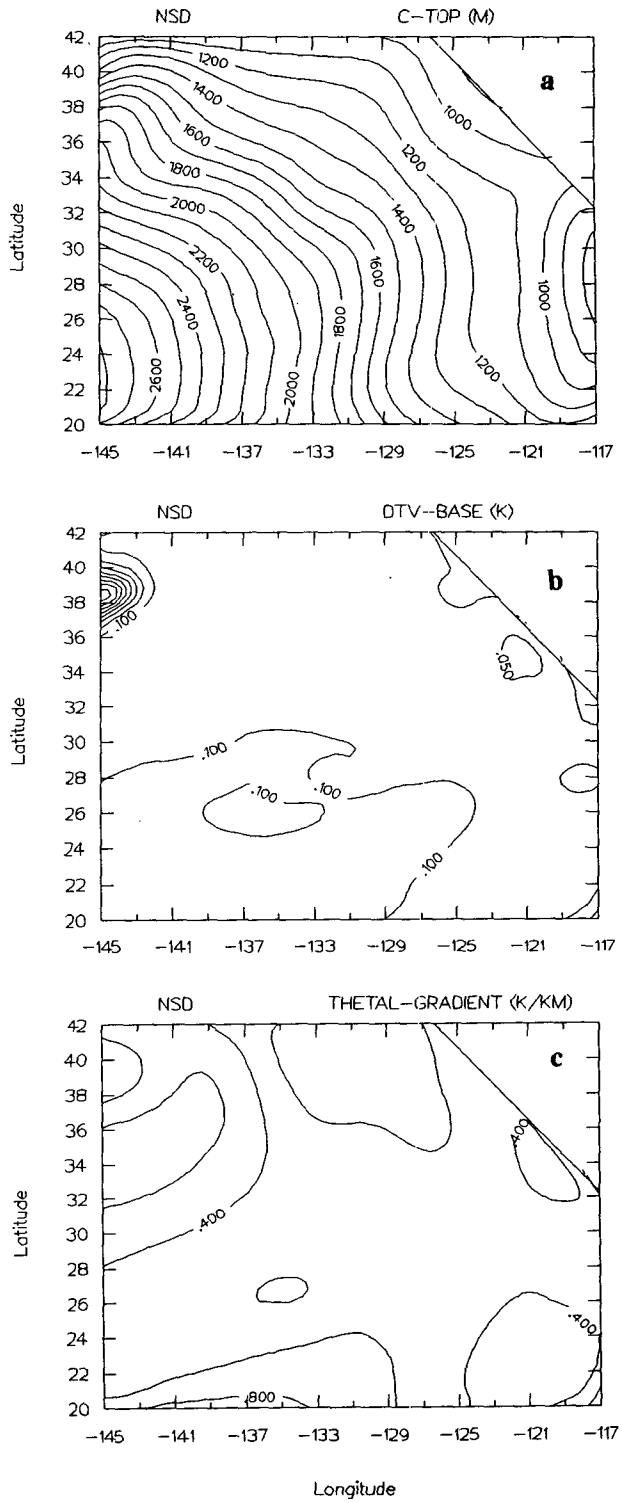

FIG. 20. Results from sensitivity experiment NSD. (a) Cloud-top heights (m); (b) θ_v discontinuities at the cloud base; (c) the gradient of θ_L (K km^{-1}) in the cloud layer.

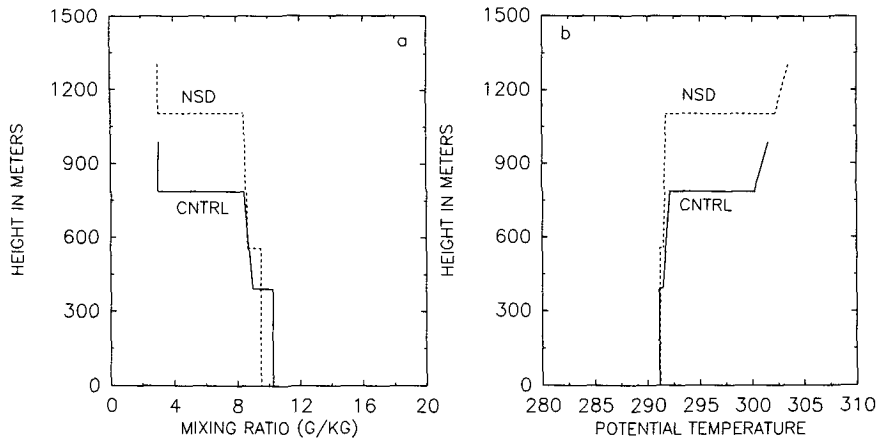

FIG. 21. The simulated vertical profiles of q in g kg^{-1} (left) and θ in K (right) at 32°N, 124°W. Solid lines denote the result of the experiment CNTRL. Dashed lines denote the result of the experiment NSD.

Cloud-top entrainment instability (CTEI) has been argued to be a process that causes the breakup of stratocumulus clouds (e.g., Randall 1980; Deardorff 1980). Recently, more restrictive criteria for CTEI have been derived and studied by Siems et al. (1990) and Siems and Bretherton (1992) and MacVean and Mason (1990). Although the present study does not consider CTEI in the breakup, it is not our intention to minimize the possible importance of CTEI for the cloud transition by this study. We simply try to explore the other possibilities that may cause this breakup.

The steady-state solutions presented in this paper are difficult to verify. A time-dependent solution could provide the transient MBL structure needed to study diurnal variations as well as to define a time-mean structure that is more compatible with averaged satellite data. In a future study, we will simulate the time-dependent characteristics of MBL clouds using time-dependent large-scale conditions provided by the ECMWF analysis and study the diurnal variation of fractional cloudiness, cloud albedo, and their influences on the surface turbulent fluxes.

It has been argued that errors in large-scale conditions, especially large-scale subsidence, may adversely affect the model's simulation of fractional cloudiness and boundary-layer structure. Thus, it is important that large-scale conditions used in the model be specified realistically. The Atlantic Stratocumulus Transition Experiment (ASTEX) of FIRE Phase II will provide substantially improved definition of the large-scale flow compared with that available in FIRE, including estimate of large-scale subsidence for the area of interest. Thus, more reliable verification and evaluation of the parameterization of MBL clouds should be obtained from the application of the model to future ASTEX datasets.

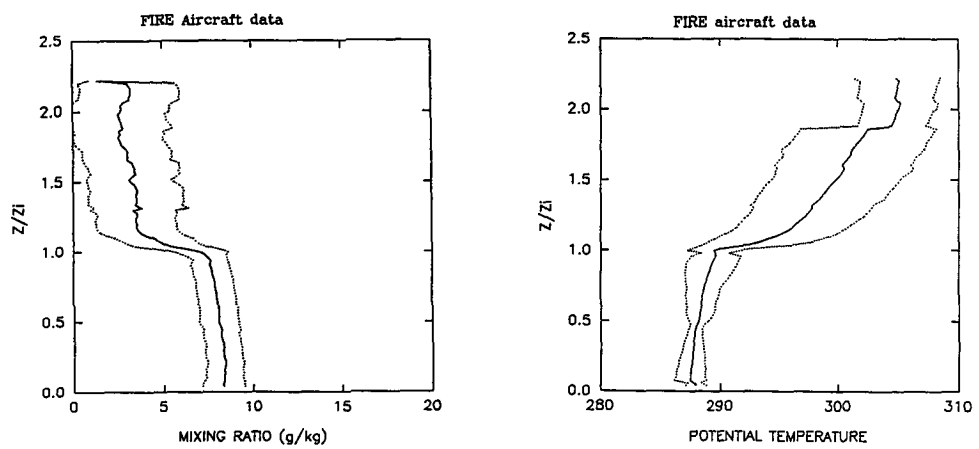

FIG. 22. Mean profiles of FIRE aircraft soundings. Position: 31.6°N, 122.4°W; SST: 17.5°C; inversion height: 880 m.

As mentioned in the Introduction, another direction for future research is to physically constrain the regional model variables using satellite-derived moisture and cloud-top height data to reduce the uncertainties in the large-scale conditions provided by other models. Thus, with more realistically resolved MBL structure, we can further evaluate the cloud parameterization scheme. More important, we can use this approach to interpret satellite data and better understand physical processes in the MBL.

Finally we would like to emphasize that the main focus of this work is to present a framework of simulating marine boundary-layer clouds using a relatively simple model with large-scale conditions provided by a large-scale meteorological model and satellite data. Although much needs to be done to improve the model, we believe that this study should prove to be a step forward to modeling and understanding marine boundary-layer clouds.

Acknowledgments. We thank Dr. Howard Hanson for providing COADS sea surface temperature data and Patrick W. Heck and David F. Young at Lockeed Engineering and Sciences Corporation for assistance in the GOES data analyses. We benefited from many discussions with Dr. Franklin Robertson. Mr. Michael Jensen kindly provided the mean profiles of aircraft soundings during FIRE (Fig. 22). This paper also benefited from comments of the reviewers. Shouping Wang was supported by NASA Grant NAS-8-37130 and NAS-8-39231. Bruce Albrecht was supported by NSF Grant ATM 89-09947 and NASA EOS Grant NAGW-2686. The satellite analyses were supported in part by the Office of Naval Research Grant USN-N000149IMP24-011.

REFERENCES

Albrecht, B. A., 1981: Parameterization of trade-cumulus cloud amounts. *J. Atmos. Sci.*, **38,** 97–105.

——, 1989: Aerosols, cloud microphysics, and fractional cloudiness. *Science,* **245,** 1227–1230.

——, 1993: The effects of precipitation on the thermodynamic structure of the trade-wind boundary layer. *J. Geophys. Res.*, **98,** 7327–7337.

——, A. K. Betts, W. H. Schubert, and S. K. Cox, 1979: A model of the thermodynamic structure of the trade wind boundary layer. Part I: Theoretical development and sensitivity tests. *J. Atmos. Sci.*, **36,** 73–89.

——, R. S. Penc, and W. H. Schubert, 1985: An observational study of cloud-topped mixed layers. *J. Atmos. Sci.*, **42,** 800–822.

——, D. A. Randall, and S. Nicholls, 1988: Observations of marine stratocumulus clouds during FIRE. *Bull. Amer. Meteor. Soc.*, **69,** 618–626.

Arakawa, A., and W. H. Schubert, 1974: Interaction of cumulus cloud ensemble with the large-scale environment. Part I. *J. Atmos. Sci.*, **31,** 674–701.

Asselin, R., 1972: Frequency filter for time integrations. *Mon. Wea. Rev.*, **100,** 487–490.

Betts, A., and W. Ridgway, 1989: A climatic equilibrium of the atmospheric boundary layer over a tropical ocean. *J. Atmos. Sci.*, **46,** 2621–2641.

——, P. Minnis, W. Ridgway, and D. F. Young, 1992: Integration of satellite and surface data using a radiative convective oceanic boundary layer model. *J. Appl. Meteor.*, **31,** 340–350.

Bougeault, Ph., 1985: The diurnal cycle of the marine stratocumulus layer: A high-order model study. *J. Atmos. Sci.*, **42,** 2826–2843.

Bretherton, C., 1993: Understanding Albrecht's model of trade cumulus cloud fields. *J. Atmos. Sci.*, **50,** 2264–2283.

Brill, K. F., and B. A. Albrecht, 1982: Diurnal variation of the undisturbed trade-wind boundary layer. *Mon. Wea. Rev.*, **110,** 601–613.

Deardorff, J. W., 1980: Cloud-top entrainment instability. *J. Atmos. Sci.*, **37,** 131–147.

Hanson, H. P., and V. E. Derr, 1987: Parameterization of radiative flux profiles within layer clouds. *J. Appl. Meteor.*, **26,** 1522–1521.

Heck, P. W., B. J. Byars, D. F. Young, P. Minnis, and E. F. Harrison, 1990: A climatology of satellite-derived cloud properties over marine stratocumulus regions. Preprints, *Conf. on Cloud Physics,* San Francisco, Amer. Meteor. Soc., J1–J7.

Kloesel, K., 1991: Marine stratocumulus cloud clearing episodes observed during FIRE. *Mon. Wea. Rev.*, **120,** 565–578.

Kuo, H.-C., and W. H. Schubert, 1988: Stability of cloud-topped boundary layers. *Quart. J. Roy. Meteor. Soc.*, **114,** 887–916.

Lilly, D. K., 1968: Models of cloud-topped mixed layers under a strong inversion. *Quart. J. Roy. Meteor. Soc.*, **94,** 292–308.

MacVean, M. K., and P. J. Mason, 1990: Cloud-top entrainment instability through small-scale mixing and its parameterization in numerical models. *J. Atmos. Sci.*, **47,** 1012–1030.

Minnis, P., and E. F. Harrison, 1984: Diurnal variability of regional cloud and clear-sky radiative parameters derived from GOES data. Part II: November 1978 cloud distributions. *J. Climate Appl. Meteor.*, **23,** 1012–1031.

——, ——, and G. G. Gibson, 1987: Cloud cover over the eastern equatorial Pacific derived from July 1983 ISCCP data using a hybrid bispectral threshold method. *J. Geophys. Res.*, **92,** 4051–4073.

——, D. R. Doelling, P. W. Heck, and D. F. Young, 1991: July climatology of marine stratocumulus clouds. *Proc. CIDOS-91 Cloud Impacts on DoD Operations and System Conf.,* El Segundo, CA, Science and Technology Corporation, 159–165.

——, P. W. Heck, D. Young, C. W. Fairall, and J. B. Snider, 1992: Stratocumulus cloud properties derived from simultaneous satellite and island-based instrumentation during FIRE. *J. Appl. Meteor.*, **31,** 317–339.

Nicholls, S. H., 1984: The dynamics of stratocumulus: Aircraft observations and comparison with a mixed-layer model. *Quart. J. Roy. Meteor. Soc.*, **110,** 783–820.

Nieburger, M., D. S. Johnson, and C. W. Chien, 1961: Studies of the structure of the atmosphere over the eastern Pacific Ocean. I: The inversion over the eastern North Pacific Ocean. *Univ. Calif. Publ. in Meteor.*, 1, University California Press, 94 pp.

Paluch, I. R., and D. H. Lenschow, 1991: Stratiform cloud formation in the marine boundary layer. *J. Atmos. Sci.*, **48,** 2141–2158.

Randall, D. A., 1980: Conditional instability of the first kind upside down. *J. Atmos. Sci.*, **37,** 148–159.

——, J. A. Coakley, Jr., C. W. Fairall, R. A. Kropfli, and D. H. Lenschow, 1984: Outlook for research on subtropical marine stratiform clouds. *Bull. Amer. Meteor. Soc.*, **65,** 1290–1301.

——, J. A. Abeles, and T. G. Corsetti, 1985: Seasonal simulation of the planetary boundary layer and boundary-layer stratocumulus clouds with a general circulation model. *J. Atmos. Sci.*, **42,** 641–676.

Robertson, F., and C. Cohen, 1990: Global analyses of water vapor, cloud and precipitation derived from a diagnostic assimilation of SSM/I geophysical retrievals. Preprints, *Fifth Conf. on Satellite Meteorology and Oceanography,* London, Amer. Meteor. Soc., 262–264.

Rogers, C. D., 1967: The use of emissivity in atmospheric radiation calculation. *Quart. J. Roy. Meteor. Soc.*, **93,** 43–54.

Schubert, W. H., J. S. Wakefield, S. K. Cox, and E. J. Steinter, 1979: Marine stratocumulus convection. Part II: Horizontally inhomogeneous solutions. *J. Atmos. Sci.*, **36,** 1308–1324.

Siems, S. T., and C. S. Bretherton, 1992: A numerical investigation of cloud-top entrainment instability and related experiments. *Quart. J. Roy. Meteor. Soc.*, **118,** 787–818.

——, ——, M. B. Baker, S. Shy, and R. Breidenthal, 1990: Buoyancy reversal and cloud-top entrainment instability. *Quart. J. Roy. Meteor. Soc.*, **116,** 705–739.

Slingo, A., 1990: Sensitivity of the earth's radiation budget to changes in low clouds. *Nature,* **343,** 49–51.

Stephens, G. A., S. Ackerman, and E. A. Smith, 1984: A shortwave parameterization revised to improve cloud absorption. *J. Atmos. Sci.*, **41,** 687–690.

Sundqvist, H., 1978: A parameterization scheme for non-convective condensation including prediction of cloud water content. *J. Roy. Meteor. Soc.*, **104,** 677–690.

Wakefield, J. S., and W. H. Schubert, 1981: Mixed-layer modeling of eastern North Pacific stratocumulus. *Mon. Wea. Rev.*, **109,** 1952–1968.

Wang, Q., and B. A. Albrecht, 1992: Convective mixing in stratocumulus-topped boundary layers observed during FIRE. *Preprint, 11th Int. Conf. on Clouds and Precipitation,* Montreal, Canada, Int. Commission on Clouds and Precipitation and Int. Association of Meteorology and Atmos. Physics, 421–424.

Wang, S., 1990: A study of diurnal variations of the stratocumulus boundary layer with a two-layer model. Preprints, *Conf. on Cloud Physics.* San Francisco, Amer. Meteor. Soc., J57–J61.

——, 1993: Modeling marine boundary layer clouds with a two-layer model: A one-dimensional simulation. *J. Atmos. Sci.*, **50,** 4001–4021.

——, and B. A. Albrecht, 1986: A stratocumulus model with an internal circulation. *J. Atmos. Sci.*, **43,** 2374–2391.